Physical properties of RE_3TMSb_5 (RE = La, Ce; TM = Ti, Zr, Hf)

by

Kai Ogasawara

B.Sc., University of British Columbia, 2014

Dissertation Submitted in Partial Fulfillment of the
Requirements for the Degree of
Master of Science

in the
Department of Physics
Faculty of Science

SIMON FRASER UNIVERSITY
Fall 2019

Approval

Name:	**Kai Ogasawara**
Degree:	**Master of Science (Physics)**
Title:	***Physical properties of RE_3TMSb_5 (RE = La, Ce; TM = Ti, Zr, Hf)***
Examining Committee:	**Chair:** Malcolm Kennett Associate Professor

Eundeok Mun
Senior Supervisor
Assistant Professor _____

Steve Dodge
Supervisor
Associate Professor _____

David Broun
Internal Examiner
Associate Professor _____

Date Defended: December 12, 2019

Abstract

Single crystals of RE_3TMSb_5 (RE = La, Ce; TM = Ti, Zr, Hf) have been grown by Sn flux and characterized by magnetization, electrical resistivity, and specific heat measurements. Powder X-ray diffraction analysis indicates that the title compounds crystallize into the hexagonal Hf_5Sn_3Cu-type structure ($P6_3/mcm$). The physical property measurements for Ce-containing compounds clearly indicate an antiferromagnetic ordering around 5 K. The effective magnetic moment estimated from magnetic susceptibility measurements is close to the theoretical value, indicating the $4f$-electrons of Ce^{3+} ions are well localized. Magnetization isotherms at $T = 2$ K show anisotropic behaviour between $H \parallel ab$ and $H \parallel c$. The temperature-dependent electrical resistivity follows a typical Kondo lattice behavior associated with thermal population of crystalline electric field (CEF) levels. The specific heat measurement for Ce-containing compounds reveals a large C_m/T value at low temperatures, which is much bigger than that of La-containing samples. At high temperatures, the CEF energy level scheme is analyzed by fitting to the Schottky peak observed in specific heat, from which the energy level splitting between the three doublet states are found to be 165 and 380 K for all three Ce-containing samples. The resistivity measurements for all La-containing samples indicate an anomalous broad peak structure at high temperatures. We also investigate the previously reported superconductivity observed in La_3TiSb_5 and Ce_3TiSb_5 below 4 K. Our resistivity and specific heat measurements show that the superconductivity is not an intrinsic property of the single crystals, and is attributed to residual Sn flux.

Keywords: Rare-earth Intermetallic Compound, Kondo Effect, RKKY Interaction

Dedication

I dedicate this thesis to my sisters and dogs.

Acknowledgements

I would like to use this section as an opportunity to thank my senior supervisor, Eundeok Mun, for all the support throughout the years. His patient guidance is what allowed me to keep advancing through the program. I would also like to thank Steve Dodge for the support and understanding of topics, as well as the completion of this writing. Lastly, to all of the professors I was fortunately able to associate with through graduate level courses and teaching assisting, "Thank you!"

We would like to acknowledge H. Park for initial sample growth. This work was supported by the Canada Research Chairs, Natural Sciences and Engineering Research Council of Canada, and Canada Foundation for Innovation program.

Table of Contents

List of Tables

List of Figures

Chapter 1

Introduction

1.1 Heavy Fermion Systems

Through specific heat and resistvity measurements, the first heavy fermion system, $CeAl_3$, was discovered [1]. A large, linear specific heat coefficient of $\gamma \sim 1620$ mJ/mol K^2 and the T^2 term in the electrical resistivity $A \sim 35$ $\mu\Omega$ cm/K^2 ($\rho = \rho_0 + AT^2$) was found in the low temperature range. Heavy fermion systems were originally defined as a collection of intermetallic compounds containing lanthanides (mainly Ce and Yb) or actinides (mainly U and Np). More compounds have been observed to exhibit such behaviour since then [2]. Heavy fermion systems gained great interest with the discovery of superconductivity in $CeCu_2Si_2$ compound [3]. The jump in specific heat at the superconducting transition temperature clearly indicates the characteristics of heavy fermion behavior. Prior to this discovery, magnetism and superconducting behaviour were believed to be contradictory phenomena. The $4f$-electrons in $CeCu_2Si_2$ are responsible for both the localized magnetic moments at high temperatures (following the Curie-Weiss law) and for superconductivity below the critical temperature T_c. A high-T_c superconductor discovered in 1986 also demonstrated that the magnetism is responsible for the superconducting phase [4]. The traditional BCS theory of superconductivity generally does not apply to these two, strongly correlated systems.

As the name suggests, heavy fermion systems are characterized by the presence of large effective mass m^* (50-1000 times greater than the mass of a free electron) below a characteristic temperature (coherence temperature) T^* [2], where the effective mass can be obtained through specific heat measurements. In the temperature range much lower than the Debye temperature and Fermi energy, the specific heat C can be expressed as $C/T = \gamma + \beta T^2$, where γ is the electronic contribution and β is the phonon contribution to the specific heat. Here, $\gamma = V_m k_F k_B^2 m^*/3\hbar^2$, V_m is the molar volume, m^* the effective mass of the electron, k_F the Fermi vector, and T is the absolute temperature. γ is on the order of 1 mJ/mol K^2 at the low temperature range for normal metals (like copper), but γ approaches very large values below the T^* for heavy fermion systems. The generally accepted definition of heavy

fermions are systems with $\gamma > 400$ mJ/mol K^2. γ is typically normalized to a mole of f-electron atoms, so comparisons between systems with different structure can be made. Some other characteristics of heavy fermion systems include (i) an enhanced Pauli spin susceptibility, indicating a large effective mass, (ii) a very large T^2 term in the electrical resistivity, (iii) the Wilson ratio between magnetic susceptibility and specific heat coefficient which is approximately one, and (iv) the Kadowaki-Wood ratio $A/\gamma^2 \sim 1 \times 10^{-5}$ $\mu\Omega$ cm mol^{2}K^2/mJ^2.

Ce- and Yb-based compounds at low temperatures show various ground states, such as antiferromagnetic and ferromagnetic ordering with weak moments, narrow-gap semiconductors with large effective masses, Fermi liquids with no long range magnetic ordering, or superconductivity [5]. Heavy fermions are Fermi liquids with no ordering while some others are non-Fermi liquids (NFL). The experimental result of Kondo alloy $Y_{1-x}U_xPd_3$ has led to intense theoretical and experimental activity in the general area of NFL behavior in d- and f-electron metals [6]. Originally, NFL behavior in d- and f-electron systems was discovered for doped systems. However, such behavior can be achieved in a variety of ways [7, 8]. The NFL state in many systems is related to a magnetic instability arising at $T = 0$, since the NFL behavior in those systems is found near a magnetically ordered phase. The NFL behaviours have been considered theoretically in the special case of a quantum phase transition (QPT) [7, 8]. A QPT is driven by a control parameter other than temperature (in contrast to classical phase transition) such as the applied magnetic field, pressure, or doping at $T = 0$. Since the experimental results can be obtained only for $T > 0$, the quantum critical point (QCP) in the phase diagram relies on the findings of the scaling behavior. Several QCP models exist for the NFL behavior of antiferromagnetic heavy fermion metals [9–17]. These models can be grouped into two categories: spin density wave quantum criticality invokes the fluctuations of the antiferromagnetic order parameter, whereas local quantum criticality involves a breakdown of the Kondo effect, changing the Fermi surface volume through the QCP. Although several theories have been proposed, there is no clear consensus about whether any particular theory explains the wide range of NFL properties.

1.1.1 Kondo Effect and RKKY Interaction

The ground state of Ce-based compounds is governed by two main interaction mechanisms, the Kondo effect and RKKY interaction. The temperature dependence of the electrical resistivity in some classes of materials showed a resistivity minimum, followed by a $-\log(T)$ dependence with decreasing temperature and saturating at low temperatures. Jun Kondo first explained the presence of a minimum in the resistivity of compounds containing d- and f-electron spins using a third-order perturbation method on a single spin-1/2 magnetic impurity (single-ion Kondo model) in 1964 [18]. The Kondo effect, named after Jun Kondo, is the screening of localized magnetic moments by the spins associated with the conduction electrons, giving rise to the $-\log(T)$ dependence above a characteristic temperature (Kondo

temperature T_K) and saturates below T_K. The resistivity minimum can be understood as a result of the decreasing phonon contribution and increasing Kondo contribution as the temperature is lowered. The Kondo contribution to the magnetic susceptibility and specific heat were derived later [19, 20]: At high temperatures, such a system follows a Curie-Weiss law, whereas at lower temperatures, the magnetic susceptibility $\chi(T)$ becomes finite with highly enhanced value; an important characteristic of heavy fermions is a large Sommerfeld coeffiecient γ in the specific heat C_P.

A system with a high occupancy of magnetic moments cannot be explained by the single-ion, Kondo model. Such a system is called a Kondo lattice, where the resistivity develops a local maximum at an another characteristic temperature (coherence temperature T_{coh}), and often follows the T^2 dependence (Fermi-liquid behavior) at even lower temperatures [21, 22]. Above T_{coh}, the interaction between the localized magnetic moments are weak, so they behave like incoherent magnetic impurities. In this range, the minimum and the $-\log(T)$ dependence occurs, much like the single-ion model. Below T_{coh}, the Kondo lattice has fully screened f-electron spins, exhibiting Fermi-liquid behaviour.

The term RKKY interaction stands for Ruderman-Kittel-Kasuya-Yosida interaction and describes the indirect magnetic exchange interactions of localized magnetic moments, mediated by the conduction electrons [23–25].

Localized magnetic moments $\langle S(x')\rangle$ of an f-electron located at x' creates Friedel oscillations in the conduction spin density $\langle\sigma(x)\rangle$ such that:

$$\langle\sigma(x)\rangle = J\chi(x-x')\langle S(x')\rangle \tag{1.1}$$

$\chi(x-x')$ represents the non-local magnetic susceptibility and J is the antiferromagnetic coupling. The spin density oscillation originates from the discontinuities in the occupancies $f(\epsilon_k)$ at the Fermi surface, and decays radially.

$$\langle\sigma(x)\rangle \approx -JD\frac{\cos(2k_Fx)}{|k_Fx|^3} \tag{1.2}$$

D represents the conduction electron density of states and x is the distance from the magnetic moment. When a second local moment $\langle S(X)\rangle$ is positioned at x, it couples to the Friedel oscillation with energy $J\langle S(x)\cdot\sigma(x)\rangle$. The RKKY Hamiltonian is given by:

$$H_{RKKY} = K\langle S(x)\cdot\sigma(x)\rangle = -J^2\chi(x-x')S(x)\cdot S(x') = J_{RKKY}(x-x')S(x)\cdot S(x') \tag{1.3}$$

$$J_{RKKY}(x-x') = J_{RKKY}(r) \approx -J^2\frac{\cos(2k_Fr)}{k_Fr} \tag{1.4}$$

The sign of the interaction is dependent on the distance between the magnetic moments, resulting in an interaction that can either be antiferromagnetic of ferromagnetic.

The ground state of Ce-based compounds can be understood by considering the RKKY interaction and Kondo screening [22]. When the RKKY coupling energy exceeds the energy required for the formation of Kondo singlets, the magnetic ordering is induced. If the Kondo screening is dominant, the ground state is a paramagnetic state. Alloys containing dilute concentrations of magnetic rare-earth or transition metal ions can demonstrate a random distribution of antiferromagnetic and ferromagnetic interactions. The magnetic state arising from such a disorder and frustration is called a "spin glass" system [26]. In this state, localized spins are frozen into random orientations. On the other hand, a dense system of magnetic ions may exhibit an antiferromagnetic or ferromagnetic state with a ordering temperature on the order of J^2D.

1.2 Theoretical Background

1.2.1 Magnetic susceptibility

The magnetic susceptibility is defined as the ratio of the magnetization M and the intensity of the applied magnetic field H [27].

$$\chi = \frac{M(H)}{H} \tag{1.5}$$

Materials with χ greater than zero are said to be paramagnetic, which aligns spins in the same direction as the applied magnetic field, whereas materials with χ less than zero are said to be diamagnetic, aligning spins in the opposite direction as the applied magnetic field.

The magnetic susceptibility of local moment systems follows a Curie-Weiss Law:

$$\frac{M}{H} = \frac{C}{T - \theta_p} \tag{1.6}$$

Here, θ_p is the Weiss temperature and the Curie constant C is defined as:

$$C = \frac{Np^2{\mu_B}^2}{3k_B}. \tag{1.7}$$

The μ_B is the Bohr magneton, k_B is the Boltzmann constant and p denotes the effective moment.

Starting with lanthanum, the ions of the rare earth elements are trivalent and demonstrates similar chemical properties. Lanthanum has zero electrons in the $4f$ shell, and the number of $4f$ electrons increases by one for each element in the rare earth group. The radii of the rare earth ions decrease through the group (this is known as the "lanthanide contraction").

From the Hund's rules, the maximum value of total spin S, the maximum value of the orbital angular momentum L, and the total angular momentum J can be determined for the

Rare-Earth Ion	Configuation	$p(calc)$	μ_{sat}
Ce^{3+}	$4f^1 5s^2 p^6$	2.54	2.14
Pr^{3+}	$4f^2 5s^2 p^6$	3.58	3.20
Nd^{3+}	$4f^3 5s^2 p^6$	3.62	3.27
Pm^{3+}	$4f^4 5s^2 p^6$	2.68	2.40
Sm^{3+}	$4f^5 5s^2 p^6$	0.84	0.71
Eu^{3+}	$4f^6 5s^2 p^6$	0	0
Gd^{3+}	$4f^7 5s^2 p^6$	7.94	7.00
Tb^{3+}	$4f^8 5s^2 p^6$	9.72	9.00
Dy^{3+}	$4f^9 5s^2 p^6$	10.63	10.00
Ho^{3+}	$4f^{10} 5s^2 p^6$	10.60	10.00
Er^{3+}	$4f^{11} 5s^2 p^6$	9.59	9.00
Tm^{3+}	$4f^{12} 5s^2 p^6$	7.57	7.00
Yb^{3+}	$4f^{13} 5s^2 p^6$	4.54	4

Table 1.1: The calculated effective moment and saturated moment of each ion in the lanthanide group.

lanthanide group ions. The effective moment $p(calc) = g[J(J+1)]^{\frac{1}{2}}$ and saturated moment $\mu_{sat} = gJ$ can be calculated by using the g factor from the Landé equation for each ion:

$$g = 1 + \frac{J(J+1) + S(S+1) - L(L+1)}{2J(J+1)}. \tag{1.8}$$

Table 1.1 summarizes the $p(calc)$ and μ_{sat} for each of the trivalent ions in the lanthanide group. Experimentally, the effective moment and Weiss temperature of rare-earth-based compounds can be extracted from a linear fit to the inverse of the magnetic susceptibility. The μ_{sat} value can be determined from the magnetization measurement as a function of external magnetic fields. Comparison of the experimental determinations of the effective moment and saturated moment with the theoretical values are useful in the analysis of new compounds, since it allows the theoretical value to be compared to the measured value. The sign of θ_p tells us where the ferromagnetic or antiferromagnetic interactions dominate - if θ_p is greater than zero, ferromagnetic, and if θ_p is less than zero, antiferromagnetic.

1.2.2 Resistivity

The electrical resistance R of an object is a quantity representing how strongly the object opposes the flow of electrical current through it. The resistance of given materials is dependent on the dimensions of the object as well as the resistivity ρ, which is a physical property of the material itself. The resistance is given by:

$$R = \rho \frac{L}{A} \tag{1.9}$$

Here, L and A represents the length and cross-sectional area of the resistor, respectively. The resistivity is temperature-dependent, and every material has a characteristic resistivity. For simple metals at low temperatures, the electrical resistivity is quadratic in temperature $\rho(T) = \rho_0 + \alpha T^2$. In general, the resistivity will not decrease all the way to zero, even at $T = 0$ K, due to the lattice imperfection, dislocation, disorder, and impurities. The residual resistivity ρ_0 reflects all these contributions. A material is called a superconductor if the electrical resistivity becomes zero below a specific, non-zero temperature, known as the critical temperature T_C.

1.2.3 Specific Heat

The specific heat C_P at constant pressure of a material is the energy required to raise the temperature of the material by 1 K per unit of mass. Specific heat measurements provide information about the electronic and magnetic properties of a material. It may also provide information about structural, magnetic, and superconducting phase transitions. Specific heat may also tell us about unwanted phases in a crystal. The heat capacity under fixed pressure is:

$$C_P = \left(\frac{dQ}{dT} \right)_P \tag{1.10}$$

In an ordinary metal at low temperatures, the C_P is characterized as a sum of the conduction electron contribution and a phonon contribution from the crystal lattice vibrations.

$$C_P = \gamma T + \beta T^3 \tag{1.11}$$

γ is known as the Sommerfeld coefficient, while the cubic term originates from the Debye T^3 approximation. By performing a linear fit on the plot of $\frac{C}{T}$ against T^2, the two parameters, γ and β, can be extracted. The Debye temperature θ_D can be estimated from $\beta = 12\pi^4 k_B / 5\theta_D^3$. The linear term reflects the effective mass of electrons. Heavy fermion materials containing elements with $4f$ or $5f$ valence electrons are characterized by γ values much larger than what is predicted by the free electron theory, as their effective masses are much larger.

In the higher temperature regime, the $C_P(T)$ approaches a constant value. This value is predicted to be $3R$ where R is the gas constant, given by the Dulong-Petit law.

The specific heat is closely related to the entropy, which is a measure of the number of available configurations. Materials containing localized magnetic moments will exhibit an additional contribution to the specific heat. To obtain the magnetic part of the specific heat, the total specific heat of a non-magnetic reference compound such as the La-based

analogue can be subtracted from the total specific heat of the magnetic compound. The magnetic specific heat C_m can be used to obtain the magnetic entropy associated with the magnetic moments of a material. The magnetic entropy S_m be found using the following integral:

$$S_m = \int_0^T dT \frac{C_m}{T}. \tag{1.12}$$

An isolated rare-earth ion with angular momentum J has $(2J + 1)$ degenerate levels. The degeneracy is lifted if an electric or magnetic field is applied. A Schottky peak in the magnetic specific heat is generally observed when the crystalline electric field levels become populated. The general expression for the Schottky contribution to the specific heat is given by:

$$C_{Sch}(T) = k_B \beta^2 \frac{\sum_{i,j} g_i g_j E_i (E_i - E_j) e^{-\beta(E_i + E_j)}}{(\sum_i g_i e^{-\beta E_i})^2} \tag{1.13}$$

β is defined as $1/k_B T$ and g_i represents the degeneracies and the E_i's represent the energy of the i-th level . For a simple two-level system, the C_{Sch} becomes:

$$C_{Sch}(T) = k_B (\beta\Delta)^2 \frac{g_0}{g_1} \frac{e^{\beta\Delta}}{(1 + (g_0/g_1)e^{\beta\Delta})^2} \tag{1.14}$$

Δ is the energy difference between g_0 and g_1. An applied magnetic field also lifts the degeneracy due to the Zeeman effect.

1.3 Previous Studies of RE_3TMSb_5

In 1995, a new group of ternary rare-earth transition-metal antimonides of the form RE_3TMSb_5 (RE = La, Ce, Pr, Nd, Sm; TM=Ti, Zr, Hf, Nb) were grown for the first time [28]. The compounds were prepared by reactions of pure powders of the rare-earth metals, transition-metals, and antimony, resulting in thin, needle-shaped crystals. Initially, this phase was discovered by analyzing arc-melted samples with diverse stoichiometric ratios of elements, where excess antimony was used to compensate vaporization of Sb. The major phase grown from this method is indeed RE_3TMSb_5 (determined by the crystal structure), but some binary antimonide phases could not be eliminated, and Sm_3NbSb_5 was unable to be grown. The structure and lattice parameters determined from x-ray diffraction were given for the first time on the newly grown title compounds. The sensitivity of the samples in air is discussed, "they begin to degrade over 1 day and completely decompose within 1 week." One of the main purposes behind the paper was "to search for new magnetic materials and to test the validity of bonding models" [28].

In 2002, the detailed characteristics of the crystal structure of the RE_3TiSb_5 family were reported [29]. Previously, only the detailed crystal structure of La_3TiSb_5 was determined

from single-crystal X-ray diffraction, with only cell parameters for the remaining members in the RE_3TiSb_5 group [28]. The samples were prepared by using powdered elements combined in stoichiometric mixtures with a total weight of 0.250 g with 0.5 g of Sn flux. The mixture was heated at 570 ^{o}C for 1 day and at 950 ^{o}C for 2 days in an evacuated fused-silica tube. The Sn flux was centrifuged, and the remaining Sn was dissolved using 6 M HCl. The lattice parameters were all determined using powder x-ray diffraction, where the hexagonal $P6_3/mcm$ space group was chosen with initial atomic positions taken from the earlier La_3TiSb_5 result.

The RE_3TiSb_5 samples were characterized by electrical resistivity and magnetization measurements [29]. Electrical resistivity from 2 to 300 K was measured along the needle axis, with an applied magnetic field perpendicular to the direction of the current. A broad structure was visible in the resistivity plots of the RE_3TiSb_5 compounds, with the curvature becoming less pronounced as the rare-earth metal is changed from La, Ce, Pr, Nd, to Sm. The compounds with La, Ce, and Nd become superconducting below 4 K, where the resistivity drop to 0 at T = 3.7 - 4.1 K was visible. The characterization of magnetic properties was made difficult as the samples were only 70-90% phase-pure. The main impurity was found to be elemental Sb, but no elemental Sn was detected.

More recently in 2017, detailed physical property measurements were conducted on Ce_3TiSb_5 [30]. Single crystals of La_3TiSb_5 and Ce_3TiSb_5 were grown using a Sn flux method. A high-purity, stoichiometric mixture of the elements of total 5 g were combined in an alumina crucible along with 10 g of Sn, then sealed in a quartz ampoule under a vacuum of 10^{-6} mbar. The mixture was heated to 1100 ^{o}C and kept there for 1 day, then cooled down to 550 ^{o}C for three weeks. The Sn flux was centrifuged out, but the formation of $CeSb_2$ was unavoidable. The specific heat measurement of a Ce_3TiSb_5 sample showed a large γ value of $\sim$598 mJ/mol K^2, which is over 60 times larger than the γ for La_3TiSb_5. Electrical resistivity Ce_3TiSb_5 clearly indicated a $-\log(T)$ dependence on temperature, demonstrating the presence of Kondo effect. The magnetization, electrical resistivity, and specific heat measurements of Ce_3TiSb_5 suggested that RKKY interaction is dominant over the Kondo interaction in the temperature range of less than 5.5 K, where the compound is in an antiferromagnetic ground state. The superconducting transition observed in both La and Ce compounds at T = 3.7 K were concluded to originate from the Sn flux in the samples.

1.4 Motivation

As far as we know, no single crystals of RE_3TMSb_5 (RE = La and Ce, TM = Zr and Hf) compounds have been previously grown and no detailed physical property measurements have been conducted on these compounds. Thus, we grew single crystals of La_3TMSb_5 and Ce_3TMSb_5 with TM = Ti, Zr, and Hf. The samples grown are indeed crystallized in the

hexagonal Hf_5Sn_3Cu-type structure ($P6_3/mcm$), confirmed from the x-ray diffraction data, which is consistent with earlier report [28]. Both La- and Ce-based samples are grown, in order to study $4f$-electron magnetism offered by the Ce^{3+} ion in the compounds. The Ti group of transition metals are chosen to observe the changes in physical properties by varying the distance between Ce-ions as we replace the Ti with Zr and Hf.

Chapter 2

Experimentals

All six of the compounds discussed in this thesis were grown using a Sn flux, where stoichiometric ratios of the elements in the target compound are placed along with Sn in an alumina crucible for growth, sealed in a silica tube. The ampoules were first heated to 1100 ^{o}C over a period of 2 hours, left to stay at 1100 ^{o}C for 4 hours, and followed by a cooling period of 198 hours down to 600 ^{o}C. The temperature profile of the furnace is shown in 2.1. The crucibles are taken out and centrifuged immediately in order to remove the Sn flux as much as possible. The grown RE_3TMSb_5 compounds form with needle-like morphology and the crystallographic c-axis is parallel to the needle axis.

In order to confirm the phase and determine lattice parameters, powder X-ray diffraction is performed on all six of the compounds in a Rigaku MiniFlex diffractometer at room temperature. Figure 2.2 summarizes the lattice parameters for all six of the grown RE_3TMSb_5 compounds along the a-axis and c-axis directions. Referenced lattice parameters are also shown for comparison [28, 29, 31]. The obtained lattice parameters and unit cell volumes are summarized in table 2.1. The DC magnetization M was measured on the samples in a Quantum Design Magnetic Property Measurement System (MPMS) in the temperature

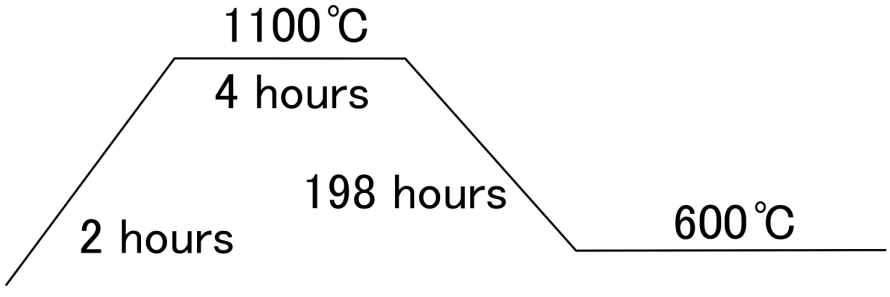

Figure 2.1: The temperature profile for the growth of single crystal RE_3TMSb_5 compounds.

RE_3TMSb_5	a (Å)	c (Å)	V (Å^3)
La_3TiSb_5	9.532	6.278	494.7
La_3ZrSb_5	9.583	6.359	505.7
La_3HfSb_5	9.577	6.348	504.2
Ce_3TiSb_5	9.425	6.228	479.1
Ce_3ZrSb_5	9.494	6.313	492.8
Ce_3HfSb_5	9.477	6.300	490.0

Table 2.1: The lattice parameters for the grown RE_3TMSb_5 compounds.

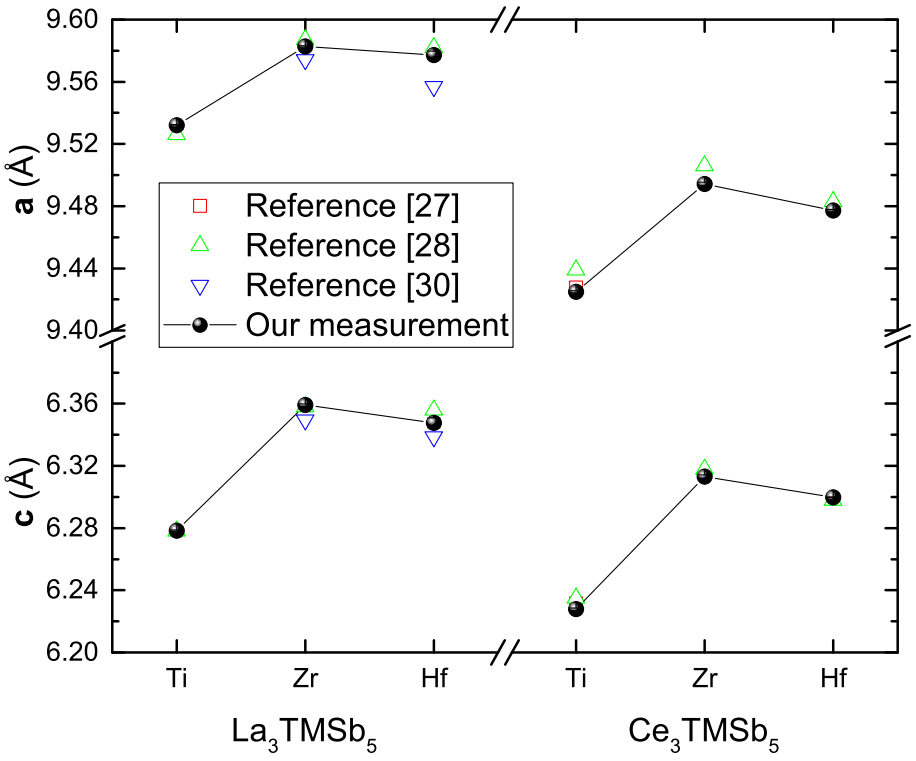

Figure 2.2: The lattice parameters of the RE_3TMSb_5 compounds.

range of 1.8 to 300 K and an applied magnetic field up to 70 kOe. The samples were mounted on clear drinking straws and measurements were taken for both $H \parallel ab$ and $H \parallel c$. The specific heat of the samples was measured by the relaxation method in a Quantum Design Physical Property Measurement System (PPMS). The electrical resistivity of the samples were measured in a Quantum Design PPMS with a temperature range of 1.8 to 300 K and applied magnetic field up to 90 kOe, measured with the current directed along the c-axis. A four probe method was used, where four platinum leads with a radius of 50 μm were attached to the needle-shaped sample using Epotek H20E silver epoxy.

Previously, RE_3TMSb_5 (RE = La, Ce, Nd) compounds were reported to undergo a superconducting phase transition below 4 K [29]. We measured the electrical resistivity of as-grown samples, which also displayed superconducting phase transitions below 4 K. This behavior is most likely associated with the Sn flux remains trapped inside, or remaining on the surface. However, after etching the samples in HCl, the phase transition disappeared in all compounds, except the Ce_3TiSb_5 sample. Figure 2.3 shows the electrical resistivity of the HCl-etched Ce_3TiSb_5 sample below $T = 10$ K with an applied field of $H = 0$ or 1 kOe. The zero-field data displays a drop below 4 K, but does not go to 0 resistivity. The resistivity not decreasing all the way to zero suggests that the superconducting behaviour is not a bulk property of Ce_3TiSb_5. Although the sample is etched in one molar HCl prior to the measurements, all of the Sn could not be thoroughly removed. The critical field of Sn is only about $H = 300$ Oe, which explains the absence of the sudden decrease in resistivity in a magnetic field of 1 kOe. As such, we think the Sn flux was embedded inside Ce_3TiSb_5 sample chosen for measurement. In addition, the specific heat measurements of all six compounds indicate no anomaly corresponding to the resistivity drop, also confirming that the phase transition is not bulk in nature. The electrical resistivity at $H = 1$ kOe for Ce_3TiSb_5 will be treated as the zero field data in the low temperature region. Our results are consistent with a recent study on RE_3TiSb_5 (RE = La and Ce), which concluded that the superconductivity is an extrinsic property arising from the Sn flux [30].

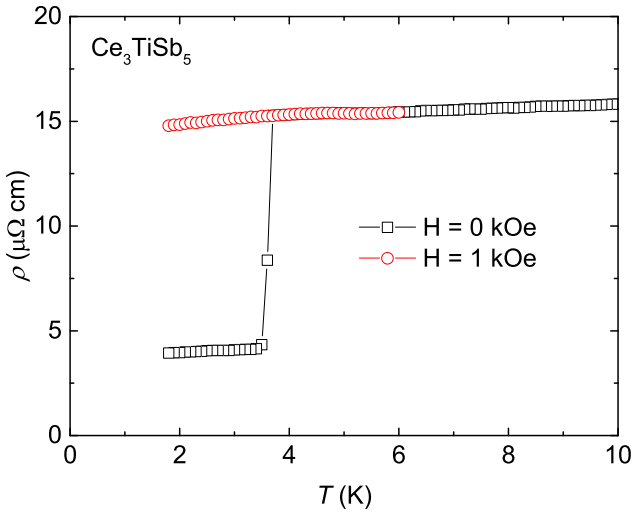

Figure 2.3: The temperature dependence of the electrical resistivity ρ for Ce_3TiSb_5 below 10 K.

Chapter 3

Results

3.1 Magnetic Susceptibility and Magnetization

3.1.1 La_3TMSb_5

The magnetic susceptibility, $\chi \equiv M/H$, for La compounds is measured in an applied magnetic field of 70 kOe along the c-axis (χ_c) and in the ab-plane (χ_{ab}) from $T = 1.8$ to 300 K. Figure 3.1 (a) presents the temperature dependence of the magnetic susceptibility for La_3TiSb_5. As the temperature increases, χ_c displays a gradual decrease between $T = 1.8$ and 50 K, where it passes a minima, then proceeds to increase gradually, approaching around -5×10^{-6} emu/f.u. at $T = 300$ K. On the other hand, χ_{ab} is decreasing in the entire, measured temperature range, approaching -3×10^{-5} emu/f.u. at $T = 300$ K. It is noted that the χ_{ab} starts above the value of χ_c in the low temperature region, but is exceeded by χ_c at $T = 100$ K where a crossover occurs.

The magnetic field dependence of magnetization, $M(H)$, along the c-axis (M_c) and in the ab-plane (M_{ab}) for La_3TiSb_5 are presented in Fig. 3.1 (b). As magnetic field increases, M_c decreases linearly to -7.5×10^{-5} μ_B/f.u. at $H = 70$ kOe. On the other hand, M_{ab} starts with a gradually increasing behaviour up to $\sim$ 20 kOe, but slightly decreases as further increasing magnetic field. The anisotropy is pronounced in the M plot, as M_{ab} is always higher than the values of M_c.

Figure 3.2 (a) presents the temperature dependence of the magnetic susceptibility for La_3ZrSb_5 in an applied field of 70 kOe. A gradual decrease between $T = 1.8$ and 225 K is seen in χ_c, then increases gradually, finally reaching around -4×10^{-5} emu/f.u. at $T = 300$ K. χ_{ab} decreases for the entire measurement range, approaching -1.1×10^{-4} emu/f.u. at $T = 300$ K. χ_{ab} begins above the value of χ_c, but is exceeded by χ_c at $T = 60$ K. This phenomena where the value of χ_c eventually exceeds the value of χ_{ab} is also observed in La_3TiSb_5.

Figure 3.2 (b) presents $M(H)$ along the c-axis and in the ab-plane for La_3ZrSb_5. M_c for La_3ZrSb_5 is similar to La_3TiSb_5. On the other hand, M_{ab} displays a broad hump from

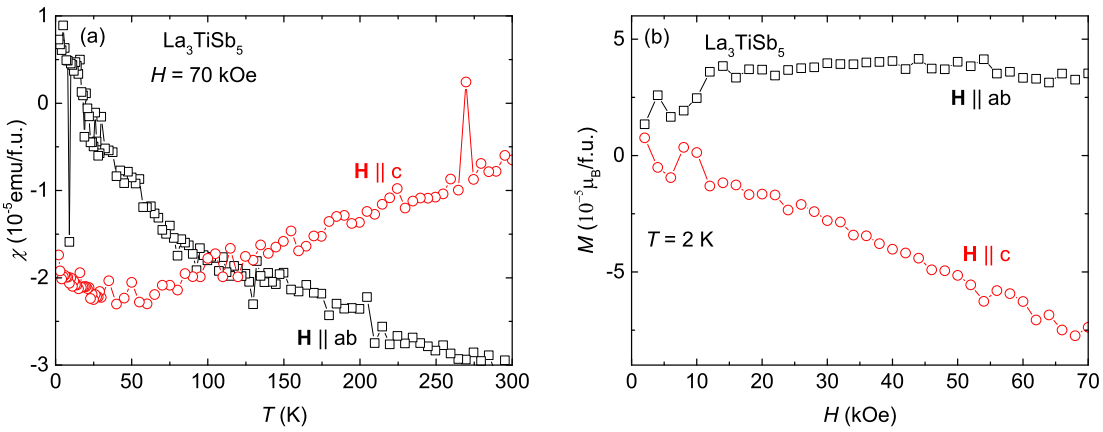

Figure 3.1: (a) The temperature dependence of the magnetic susceptibility χ for La_3TiSb_5. (b) The field dependence of the magnetization M of La_3TiSb_5.

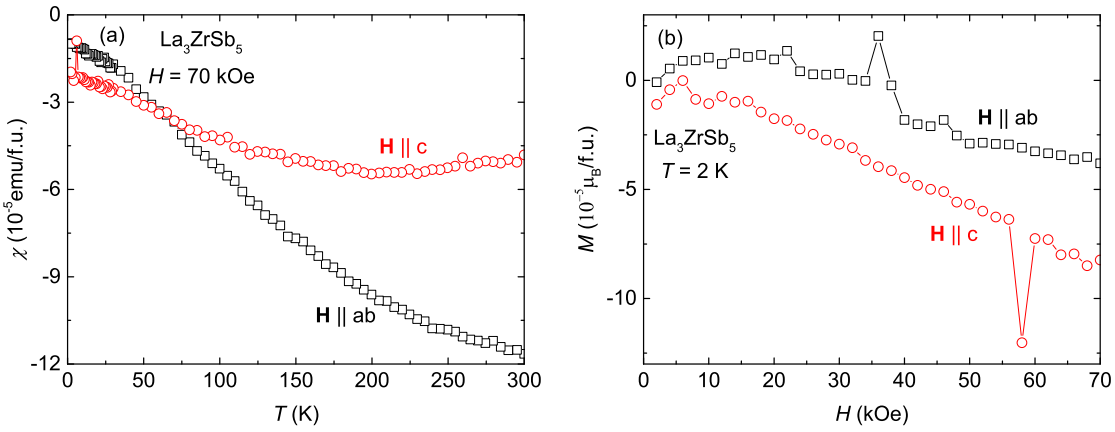

Figure 3.2: (a) The temperature dependence of the magnetic susceptibility χ for La_3ZrSb_5. (b) The field dependence of the magnetization M of La_3ZrSb_5.

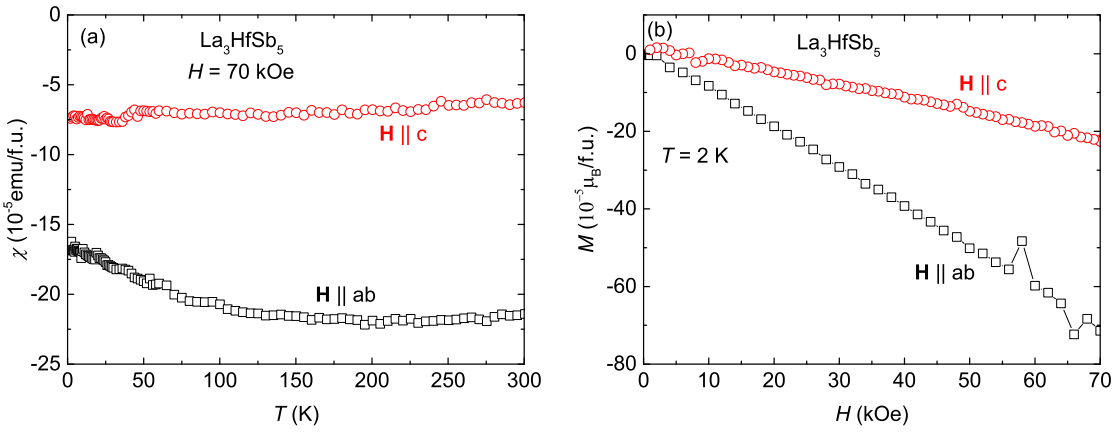

Figure 3.3: (a) The temperature dependence of the magnetic susceptibility χ for La_3HfSb_5. (b) The field dependence of the magnetization M of La_3HfSb_5.

$H = 0$ to 40 kOe, and a smooth decrease above $H = 40$ kOe to -4×10^{-5} μ_B/f.u. at $H =$ 70 kOe. M_{ab} is always greater than the values of M_c. This behaviour in M for La_3ZrSb_5 is similar to what is seen in La_3TiSb_5.

χ_c and χ_{ab} for La_3HfSb_5 measured in an applied field of 70 kOe are shown in figure 3.3 (a). χ_c displays a subtle, gradual increase for the entire temperature range of $T = 1.8$ to 300 K, which is almost flat on the scale shown in figure 3.3. On the other hand, χ_{ab} displays a gradual decrease until around $T = 200$ K, where it begins to flatten, reaching a value of -2.2×10^{-4} emu/f.u. at $T = 300$ K. In La_3TiSb_5 and La_3ZrSb_5, χ_{ab} began lower than χ_c, and eventually exceeded χ_c at some temperature, whereas χ_c is greater than χ_{ab} for the temperature range of $T = 1.8$ to 300 K for La_3HfSb_5.

$M(H)$ for La_3HfSb_5 along the c-axis and in the ab-plane are presented in figure 3.3 (b). M_c decreases linearly to -2×10^{-4} μ_B/f.u. at $H = 70$ kOe. This behaviour of M_c for La_3HfSb_5 is similar to La_3TiSb_5 and La_3ZrSb_5. Somewhat similarly to M_c, M_{ab} displays a linear decrease from 0 and approaching -7×10^{-4} μ_B/f.u. at $H = 70$. In La_3TiSb_5 and La_3ZrSb_5, M_{ab} did not demonstrate a linearly decreasing behaviour throughout the applied field range of $H = 0$ to 70 kOe, like what is seen in the La_3HfSb_5. It is noted that M_{ab} is greater than M_c for La_3HfSb_5 between $H = 0$ to 70 kOe, but this is not the case for La_3TiSb_5 and La_3ZrSb_5.

3.1.2 Ce_3TiSb_5

Figure 3.4 presents the temperature dependence of the inverse magnetic susceptibility, χ_c^{-1} and χ_{ab}^{-1}, measured in an applied field of 1 kOe for Ce_3TiSb_5, which is consistent with earlier report [30]. The inverse magnetic susceptibility curves increase linearly above 175 K for χ_c and above 150 K for χ_{ab}. The solid lines represents fits to the Curie-Weiss law: $\chi = C/(T - \theta_p)$, where C is the Curie constant and θ_p is the Weiss temperature. From the

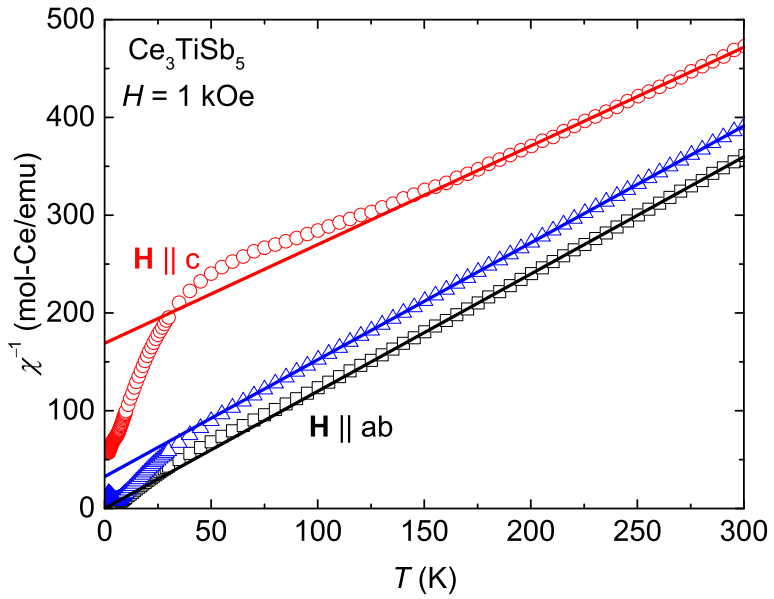

Figure 3.4: The temperature dependence of the inverse magnetic susceptibility χ^{-1} for Ce_3TiSb_5. The solid lines represents fits to the Curie-Weiss law. The open circular, square, and triangular symbols represent χ_c, χ_{ab}, and the polycrystalline average, respectively.

		μ_{eff} (μ_B/Ce)	θ_p (K)
Ce_3TiSb_5	χ_c	2.81	-168
	χ_{ab}	2.58	0
	χ_{poly}	2.59	-27
Ce_3ZrSb_5	χ_c	2.85	-172
	χ_{ab}	2.58	-5
	χ_{poly}	2.60	-32
Ce_3HfSb_5	χ_c	2.79	-169
	χ_{ab}	2.60	-3
	χ_{poly}	2.59	-30

Table 3.1: The effective moment μ_{eff} and Curie-Weiss temperature θ_p for the Ce_3TMSb_5 (TM = Ti, Zr, Hf) samples. The values are obtained from a linear fit performed on the inverse magnetic susceptibility plot, χ_c^{-1}, χ_{ab}^{-1}, and χ_{poly}^{-1}.

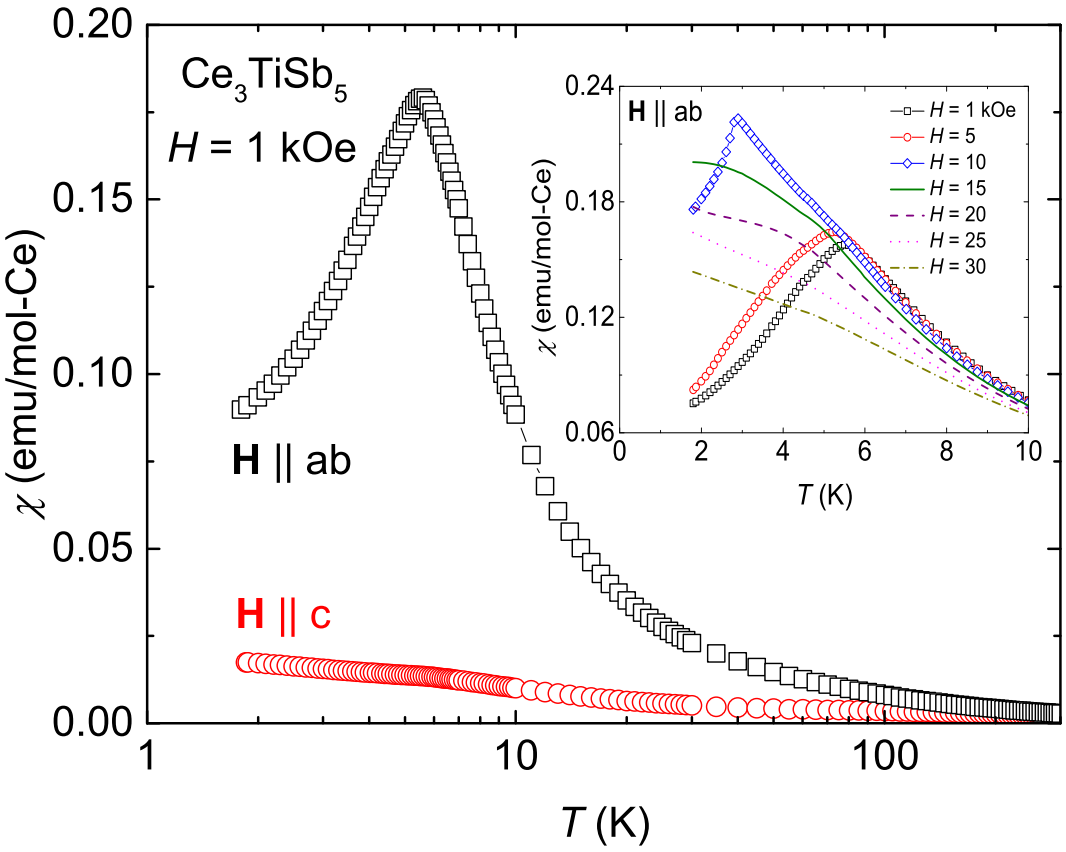

Figure 3.5: The temperature dependence of the magnetic susceptibility χ for Ce_3TiSb_5. In the inset, the temperature dependence of χ_{ab} is presented for applied magnetic fields of H = 1, 5, 10, 15, 20, 25, and 30 kOe.

fit, the effective moment μ_{eff} and Weiss temperature are estimated to be $\mu_{eff} = 2.81\ \mu_B$/Ce and θ_p = -168 K for $H||c$ and $\mu_{eff} = 2.58\ \mu_B$/Ce and $\theta_p = 0$ K for $H||ab$. The μ_{eff} and θ_p values for the Ce-containing compounds are summarized in table 3.1. The significant difference between the obtained θ_p for $H||c$ and $H||ab$ is most likely associated with the crystalline electric field effect. The μ_{eff} and θ_p are also estimated from the polycrystalline average of the magnetic susceptibility, $\chi_{poly} \equiv \frac{1}{3}\chi_c + \frac{2}{3}\chi_{ab}$. The obtained value of $\mu_{eff} = 2.59\ \mu_B$ for χ_{poly} is close to the theoretical value $\mu_{eff} = 2.54\ \mu_B$ for the free Ce^{3+} ion, indicating that the Ce atoms in the Ce_3TiSb_5 compound are in the Ce^{3+} state. For χ_{poly}, the Weiss temperature is found to be a negative value of θ_p = -27 K, indicating antiferromagnetic exchange interactions between the Ce^{3+} ions.

The magnetic susceptibility curves along the c-axis and in the ab-plane are shown in figure 3.5 in a semi-log scale. The magnitude of both χ_c and χ_{ab} for Ce_3TiSb_5 is about four orders of magnitude greater than the values measured for La_3TiSb_5. In the low temperature regime, below 100 K, a large anisotropy is observed between χ_c and χ_{ab}. χ_{ab} indicates a

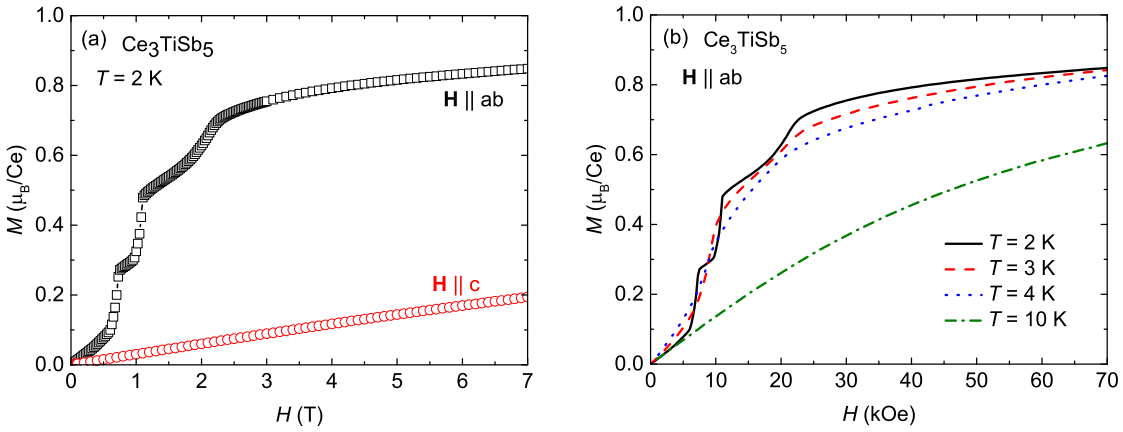

Figure 3.6: (a) The field dependence of the magnetization M of Ce_3TiSb_5. The data displayed with open symbols and solid lines represents measurements conducted under an increasing magnetic field and a decreasing magnetic field, respectively. (b) The M_{ab} data for Ce_3TiSb_5 is presented for temperatures T = 2, 3, 4, and 10 K.

peak at T = 5.6 K, whereas χ_c shows a kink at the same temperature. The peak in χ_{ab} suggests that there is an antiferromagnetic ordering below $T_N \sim$ = 5 K, determined by the peak position in $d(\chi T)/dT$ analysis. The inset of figure 3.5 displays the temperature dependence of χ_{ab} for H = 1, 5, 10, 15, 20, 25, and 30 kOe. As the applied magnetic field is increased, the peak observed at H = 1 kOe shifts to a lower temperature, and is eventually suppressed below T = 2 K. The $\chi_{ab}(T)$ behaviour changes for applied fields above H = 15 kOe. For the H = 15, 20, and 25 kOe data, no peak is detected, but a broad hump is seen instead. Broad humps are observed in the H = 15 kOe data at $T \sim$ 3 and 5 K. Similarly, a broad structure is seen in the H = 20 kOe data at $T \sim$ 4.5 K, while a very subtle change in slope can be seen in the H = 25 kOe data around $T \sim$ 4.5 K. As the applied field is further increased to H = 30 kOe, no broad structures are observed, indicating that the antiferromagnetic ordering is completely suppressed below 2 K.

Figure 3.6 (a) shows the field dependence of magnetization, M_c and M_{ab}, for Ce_3TiSb_5. A large anisotropy in the magnetization M is observed. M_c increases linearly, up to almost 0.2 μ_B/Ce at H = 70 kOe, whereas M_{ab} shows steps involving metamagnetic transitions at H = 7, 11, 21 kOe, which are determined by dM/dH analysis. This result is consistent with earlier study [30]. It is noted that M_{ab} approaches a value around 0.85 μ_B/Ce at H = 70 kOe, which is only 40% of the theoretical, free ion saturation moment of Ce^{3+} (2.14 μ_B/Ce). Both M_c and M_{ab} are measured with an increasing and decreasing field, but no observable hysteresis is detected. The field dependence of M_{ab} measured at T = 2, 3, 4, and 10 K are presented in figure 3.6 (b). As the temperature is increased to T = 3 K, the metamagnetic transitions visible at T = 2 K becomes less pronounced. Changes in the slope are seen at H = 10 and 21 kOe in the T = 3 K data, albeit subtle in comparison to the T = 2 K data. At T = 4 K, the step-like behaviour is even further broadened, with a change

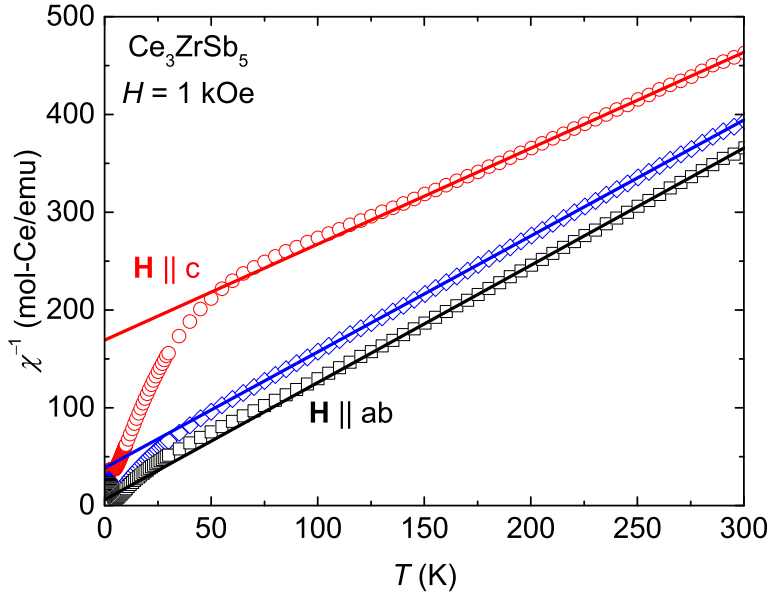

Figure 3.7: The temperature dependence of the inverse magnetic susceptibility χ^{-1} for Ce_3ZrSb_5. The solid lines represents fits to the Curie-Weiss law. The open circular, square, and triangular symbols represent χ_c, χ_{ab}, and the polycrystalline average, respectively.

in dM/dH observed at $H = 9$ and 19 kOe. At $T = 10$ K, the metamagnetic transitions are no longer observed.

3.1.3 Ce_3ZrSb_5

The temperature dependence of χ_c^{-1} and χ_{ab}^{-1} for Ce_3ZrSb_5 is presented in figure 3.7. A linear fit is performed on the inverse magnetic susceptibility data above 175 K for χ_c and above 150 K for χ_{ab}. The values $\mu_{eff} = 2.85\ \mu_B$/Ce and θ_p = -172 K for $H||c$ and $\mu_{eff} = 2.58\ \mu_B$/Ce and θ_p = -5 K for $H||ab$ are obtained from the linear fits to the Curie-Weiss law. Similar to the Ce_3TiSb_5, Ce_3ZrSb_5 displays a significant difference between the obtained θ_p for $H||c$ and $H||ab$. The obtained value of $\mu_{eff} = 2.60\ \mu_B$ for χ_{poly} is close to the theoretical value for the free Ce^{3+} ion. For χ_{poly}, the Weiss temperature is found to be a negative value of θ_p = -32 K, indicating antiferromagnetic exchange interactions between the Ce^{3+} ions in Ce_3ZrSb_5, which is also seen in Ce_3TiSb_5.

Figure 3.8 shows the magnetic susceptibility curves along the c-axis and in the ab-plane. χ_{ab} indicates a peak at $T = 5.1$ K, whereas χ_c shows a kink at the same temperature. The peak in χ_{ab} suggests that there is an antiferromagnetic ordering below 5.1 K. In the inset of figure 3.8, the temperature dependence of χ_{ab} for H = 1, 2.5, 5, 10, 15, and 20 kOe are shown. The peak observed at $H = 1$ kOe shifts to a lower temperature with increasing field, and is eventually suppressed below $T = 2$ K for $H > 20$ kOe.

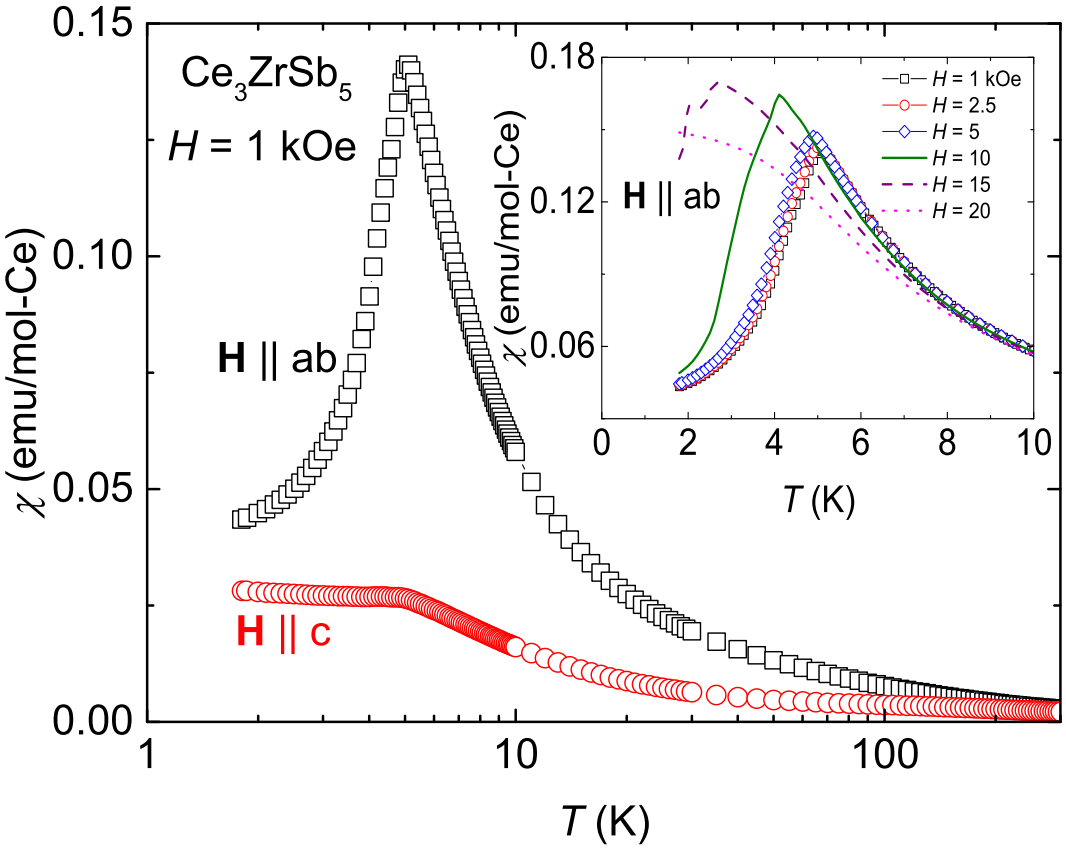

Figure 3.8: The temperature dependence of the magnetic susceptibility χ for Ce_3ZrSb_5. In the inset, the temperature dependence of χ_{ab} is presented for applied magnetic fields of H = 1, 2.5, 5, 10, 15, and 20 kOe.

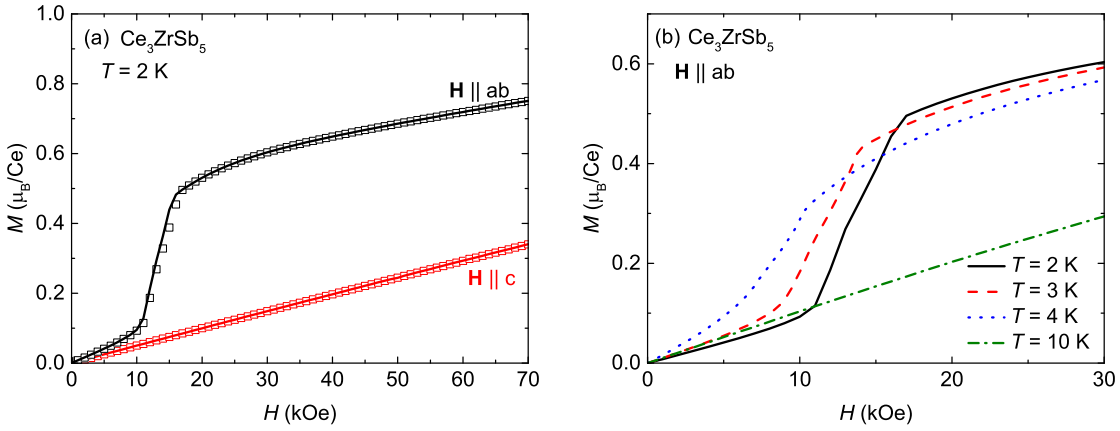

Figure 3.9: (a) The field dependence of the magnetization M of Ce_3ZrSb_5. The data displayed with open symbols and solid lines represents measurements conducted under an increasing magnetic field and a decreasing magnetic field, respectively. (b) The M_{ab} data for Ce_3ZrSb_5 is presented for temperatures T = 2, 3, 4, and 10 K.

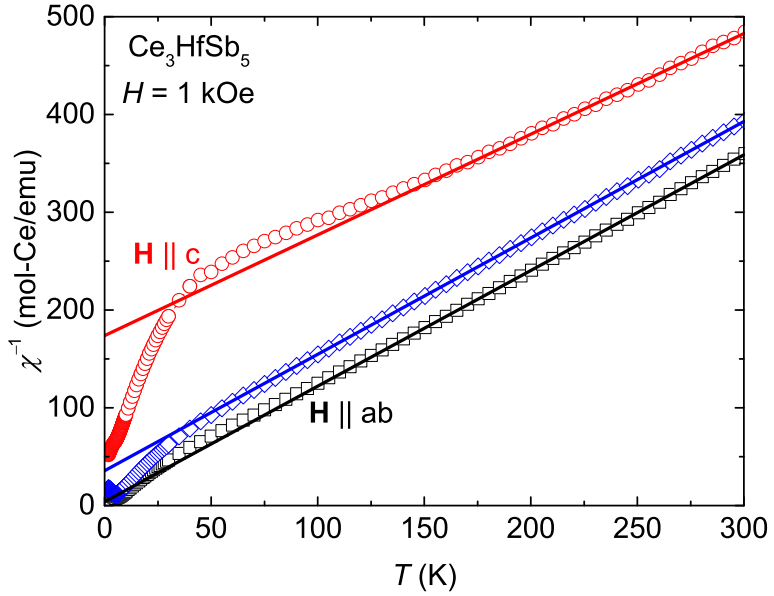

Figure 3.10: The temperature dependence of the inverse magnetic susceptibility χ^{-1} for Ce_3HfSb_5. The solid lines represents fits to the Curie-Weiss law. The open circular, square, and triangular symbols represent χ_c, χ_{ab}, and the polycrystalline average, respectively.

The field dependence of magnetization for Ce_3ZrSb_5 are presented in figure 3.9 (a). M_c increases linearly, up to 0.35 μ_B/Ce at H = 70 kOe, whereas M_{ab} shows a jump at H = 12 kOe. In Ce_3TiSb_5, multiple steps representing metamagnetic transitions are observed in $M(H)$, but only one step is observed in Ce_3ZrSb_5. M_{ab} approaches a value around 0.75 μ_B/Ce at H = 70 kOe, which is lower than the free ion saturation moment of Ce^{3+}. Figure 3.9 (b) presents the field dependence of M_{ab} measured at T = 2, 3, 4, and 10 K. As the temperature is increased to 4 K, the steps become less pronounced, similar to what is seen in the Ce_3TiSb_5 data. The step is no longer observed at 10 K, and the field dependence becomes linear.

3.1.4 Ce_3HfSb_5

Figure 3.10 shows the temperature dependence of the inverse magnetic susceptibility for Ce_3HfSb_5. From the fit to the Curie-Weiss law, the values μ_{eff} = 2.79 μ_B/Ce and θ_p = -169 K for $H||c$ and μ_{eff} = 2.60 μ_B/Ce and θ_p = -3 K for $H||ab$ are found. The significant difference between the obtained θ_p for $H||c$ and $H||ab$ is clearly visible in Ce_3TiSb_5 and Ce_3ZrSb_5 data as well, and is most likely attributed to the crystalline electric field effect. For χ_{poly}, the values μ_{eff} = 2.59 μ_B and θ_p = -30 K are obtained. For all three of the Ce-containing compounds, the μ_{eff} is close to the the theoretical value 2.54 μ_B, indicating that the Ce atoms in the Ce_3TMSb_5 compounds are in the Ce^{3+} state.

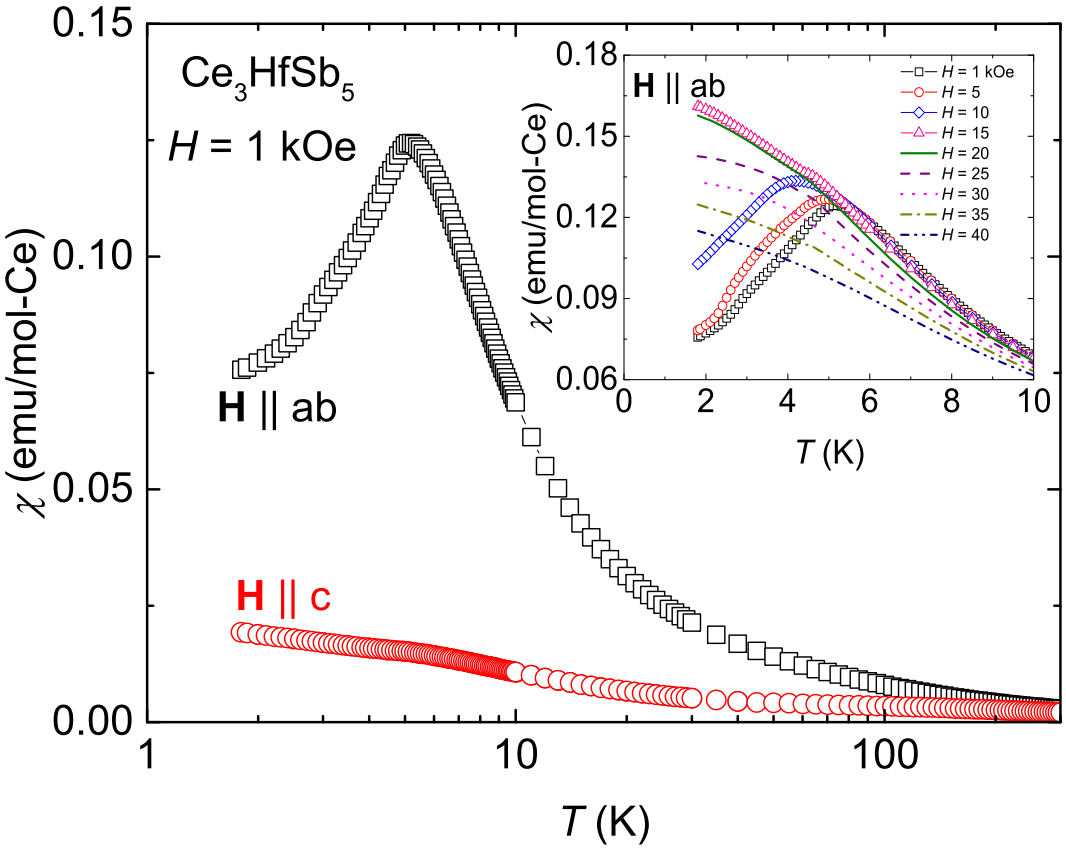

Figure 3.11: The temperature dependence of the magnetic susceptibility χ for Ce_3HfSb_5. In the inset, the temperature dependence of χ_{ab} is presented for applied magnetic fields of H = 1, 5, 10, 15, 20, 25, 30, 35, and 40 kOe.

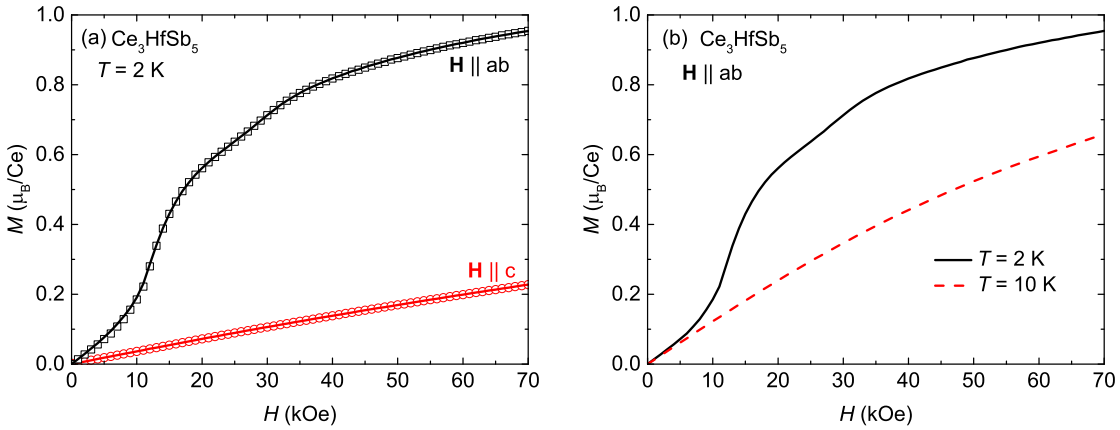

Figure 3.12: (a) The field dependence of the magnetization M of Ce_3HfSb_5. The data displayed with open symbols and solid lines represents measurements conducted under an increasing magnetic field and a decreasing magnetic field, respectively. (b) The M_{ab} data for Ce_3HfSb_5 is presented for temperatures $T = 2$ and 10 K.

χ_c and χ_{ab} for Ce_3HfSb_5 are shown in figure 3.11. Below 100 K, a large anisotropy is observed between χ_c and χ_{ab}, which is also demonstrated by Ce_3TiSb_5 and Ce_3ZrSb_5. χ_{ab} shows a peak at $T = 5.2$ K, whereas χ_c shows a kink at the same temperature. The peak in χ_{ab} is evidence that antiferromagnetic ordering occurs below 5.2 K. The temperature dependence of χ_{ab} for $H = 1$, 5, 10, 15, 20, 25, 30, 35, and 40 kOe is shown in figure 3.11. As the applied magnetic field is increased, the peak observed at $H = 1$ kOe moves towards a lower temperature. The $\chi_{ab}(T)$ behaviour changes above $H = 15$ kOe, as no peak is detected, but a broad hump is seen instead. As the applied field is further increased, the hump becomes less pronounced, and finally no longer observable at $H = 40$ kOe. The suppression of the peak below $T = 2$ K with an increasing field is also observed in the Ce_3TiSb_5 and Ce_3ZrSb_5 samples.

$M_c(T)$ and $M_{ab}(T)$ for Ce_3HfSb_5 are shown in figure 3.12 (a). M_c increases linearly, up to 0.22 μ_B/Ce at $H = 70$ kOe, whereas M_{ab} shows slope changes at $H = 12$ and 28 kOe. It is noted that M_{ab} approaches a value around 0.95 μ_B/Ce at $H = 70$ kOe, which is significantly lower than the free ion saturation moment of Ce^{3+}. Both M_c and M_{ab} is measured with an increasing and decreasing field, but no hysteresis is observed. The field dependence of M_{ab} measured at $T = 2$ and 10 K are presented in figure 3.12 (b). As the temperature is increased to $T = 10$ K, the slope changes detected at $T = 2$ K disappears, and the field dependence becomes smooth.

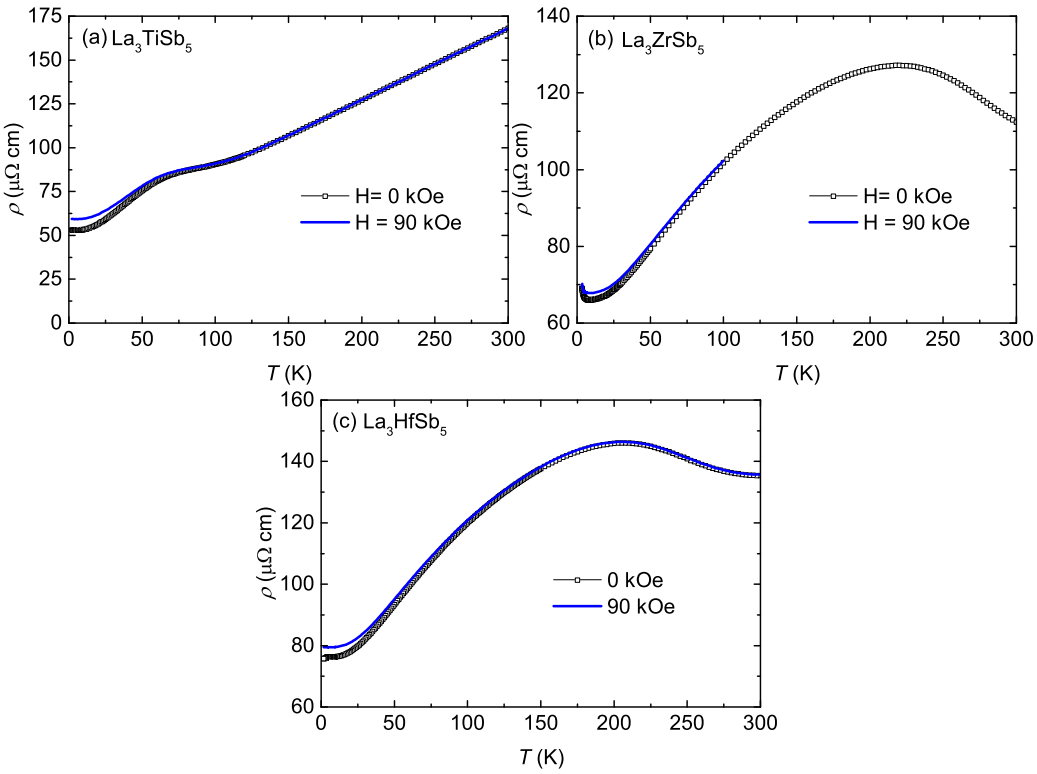

Figure 3.13: (a), (b), and (c) shows the temperature dependence of the electrical resistivity ρ for La_3TiSb_5, La_3ZrSb_5, and La_3HfSb_5, respectively, with the current directed along the c-axis.

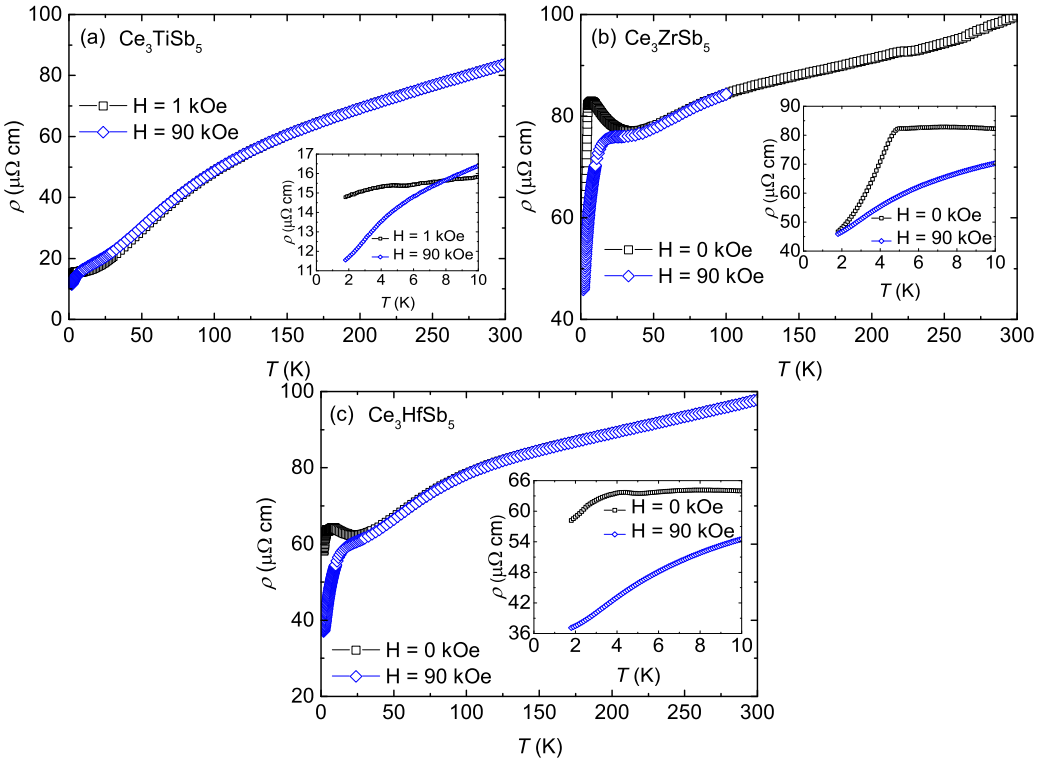

Figure 3.14: (a), (b), and (c) shows the temperature dependence of the electrical resistivity ρ for Ce_3TiSb_5, Ce_3ZrSb_5, and Ce_3HfSb_5, respectively, with the current directed along the c-axis. The insets show the low temperature region of ρ, $T \leqslant 10$ K for Ce_3TiSb_5 and Ce_3ZrSb_5 and $T \leqslant 35$ K for Ce_3HfSb_5.

3.2 Resistivity

3.2.1 La_3TMSb_5 (TM = Ti, Zr, Hf)

Figure 3.13 (a), (b), and (c) shows the temperature dependence of electrical resistivity $\rho(T)$ for La_3TMSb_5 (TM = Ti, Zr, and Hf). In zero field, the $\rho(T)$ for all three compounds follows a metallic behavior, but with a broad peak structure at high temperatures around ∼75 K for TM = Ti, ∼220 K for Zr, and ∼210 K for Hf. At low temperatures, $\rho(T)$ for TM = Ti and Hf shows a saturation behavior, whereas $\rho(T)$ for TM = Zr indicates an upturn below 10 K. The $\rho(T)$ at $H = 90$ kOe for all three compounds shows a small, positive magnetoresistance at low temperatures.

3.2.2 Ce_3TMSb_5 (TM = Ti, Zr, Hf)

The temperature dependence of the electrical resistivity, $\rho(T)$, for Ce_3TiSb_5 is shown in figure 3.14 (a). In zero field, the $\rho(T)$ curve above $T = 10$ K displays a gradual increase, all

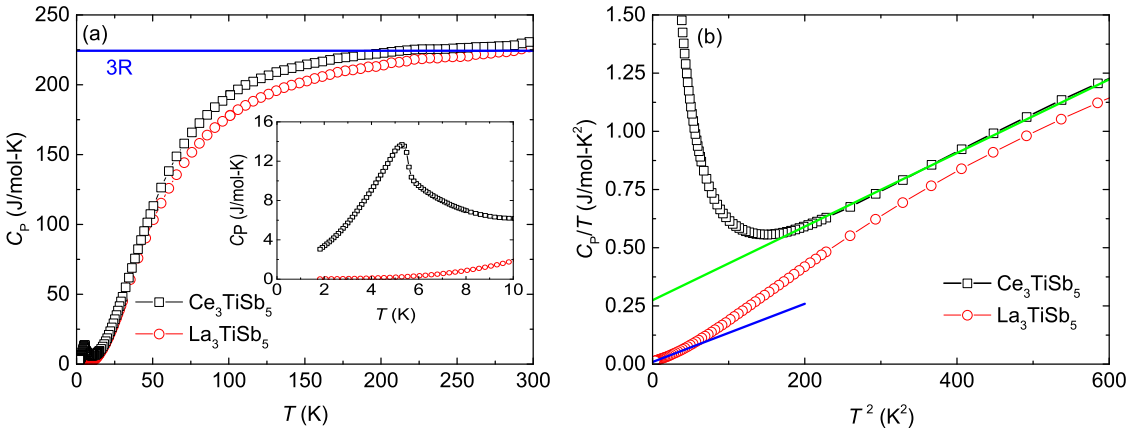

Figure 3.15: (a) The temperature dependence of specific heat $C_P(T)$ for La_3TiSb_5 and Ce_3TiSb_5. The solid line represents the calculated Dulong-Petit limit value, $C_P = 224.3$ J/mol-K. The inset shows the temperature dependence of C_P for La_3TiSb_5 and Ce_3TiSb_5 in the low temperature region. (b) C_P/T for La_3TiSb_5 and Ce_3TiSb_5 are shown. The solid lines represent the linear fit used to obtain the γ and β values.

the way up to $T = 300$ K, with a broad hump centred around $T = 100$ K. This temperature dependence is typical for the Kondo lattice compounds. The $\rho(T)$ below $T = 10$ K is shown in the inset of figure 3.14 (a). A minimum in the resistivity is seen around $\sim$5 K, followed by a broad maximum around $\sim$4 K. The derivative of the electrical resistivity with respect to the temperature, $d\rho(T)/dT$, in the low temperature region clearly shows a pronounced minimum at $T = 5.2$ K (see discussion), which corresponds to the peak position in the magnetic susceptibility. The low temperature broad feature observed in the resistivity is completely suppressed by external magnetic field of $H = 90$ kOe.

Figure 3.14 (b) and (c) presents the $\rho(T)$ for Ce_3ZrSb_5 and Ce_3HfSb_5, respectively. The $\rho(T)$ curves for both compounds follow typical Kondo lattice behavior. Unlike the Ce_3TiSb_5, a shallow minimum in the resistivity curve is clearly visible at $T = 37$ K for Ce_3ZrSb_5 and $T = 25$ K for Ce_3HfSb_5. At low temperatures, $\rho(T)$ for Ce_3ZrSb_5 demonstrates a kink as a signature of phase transition as shown in the inset of figure 3.14 (b). The resistivity curve for Ce_3HfSb_5 displays a sharp increase up to $T = 4.4$ K, where a peak is attained, with a dip at $T = 5.1$ K. From there, ρ increases again to reach another peak at $T = 7.5$ K (inset (c)). The curve decreases until a shallow minima is approached around $T = 25$ K. The phase transition temperature is determined from the $d\rho/dT$ analysis (see discussion). In the $H = 90$ kOe data, the anomalies displayed by the $H = 0$ data is suppressed.

3.3 Specific Heat

3.3.1 La_3TiSb_5 and Ce_3TiSb_5

The temperature dependence of specific heat, $C_P(T)$, for La_3TiSb_5 and Ce_3TiSb_5 are shown in figure 3.15 (a). The $C_P(T)$ curves for both compounds reaches $\sim$ 224 J/mol-K at 300 K, which is close to the Dulong-Petit limit [27]. It is noted that the $C_P(T)$ for Ce_3TiSb_5 is greater than La_3TiSb_5 below 300 K, where the difference can be attributed to the electronic Schottky contributions. The inset of figure 3.15 (a) shows $C_P(T)$ in the low temperature region, where the two compounds behave differently. The $C_P(T)$ for La_3TiSb_5 smoothly decreases to zero as the temperature is decreased, whereas Ce_3TiSb_5 has a pronounced peak at T = 5.3 K, indicating an antiferromagnetic transition. The difference in $C_P(T)$ between the two compounds is most likely associated with the magnetic Ce^{3+} moments, as the two compounds are isostructural. Figure 3.15 (b) shows the C_P/T plotted against T^2 for La_3TiSb_5 and Ce_3TiSb_5. The solid lines represent fits to the $C_P(T) = \gamma T + \beta T^3$. The γ = 275 mJ/mol-K^2 for Ce_3TiSb_5 is significantly bigger than the γ = 9.45 mJ/mol-K^2 for La_3TiSb_5. The estimated Debye temperature θ_D is 223 K for both La_3TiSb_5 and Ce_3TiSb_5. Table 3.2 summarizes the γ and Debye temperature θ_D found by performing linear fits on the high-temperature regions of $C_P(T)/T$ for each of the RE_3TMSb_5 compounds. It is noted that the γ values for the Ce-based compounds are overestimated, as the fits are conducted over a much wider temperature range in comparison to the La-based compounds. The specific heat measurements for both La_3TiSb_5 and Ce_3TiSb_5 compounds are consistent with the earlier report [30].

3.3.2 La_3ZrSb_5 and Ce_3ZrSb_5

$C_P(T)$ for La_3ZrSb_5 and Ce_3ZrSb_5 are shown in figure 3.16 (a). Similarly to the Ti-based compounds, the obtained specific heat curves for both compounds approach a value close to the Dulong-Petit limit at 300 K and the C_P of Ce_3ZrSb_5 is slightly greater than that of La_3ZrSb_5 below 300 K. At low temperatures, the $C_P(T)$ of La_3ZrSb_5 demonstrates a smooth decrease to zero as the temperature is decreased, whereas a peak is seen in Ce_3ZrSb_5 at T = 4.7 K with a kink at T = 4.3 K as shown in the inset of figure 3.16 (a). The γ values are extracted from a linear fit on C_P/T vs T^2, as shown in the figure 3.16 (b), where γ = 235 mJ/mol-K^2 and γ = 10.84 J/mol-K^2 for Ce_3ZrSb_5 and La_3ZrSb_5, respectively. The obtained Debye temperatures θ_D = 233 K for La_3ZrSb_5 and θ_D = 213 K for Ce_3ZrSb_5 are similar to the values obtained for the Ti-based compounds.

3.3.3 La_3HfSb_5 and Ce_3HfSb_5

Figure 3.17 (a) presents the specific heat for La_3HfSb_5 and Ce_3HfSb_5. Both compounds are in good agreement with the Dulong-Petit law, as they approach the expected value at T =

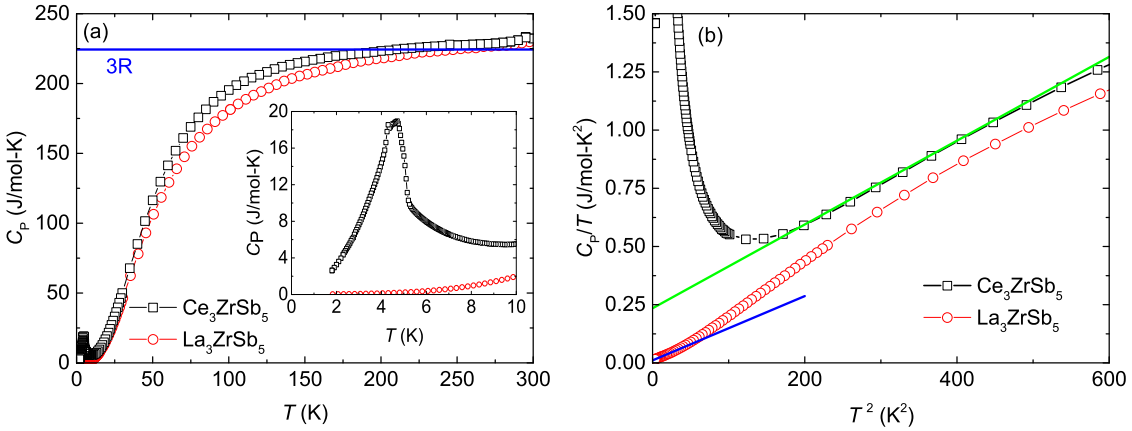

Figure 3.16: (a) The temperature dependence of specific heat $C_P(T)$ for La_3ZrSb_5 and Ce_3ZrSb_5. The solid line represents the calculated Dulong-Petit limit value, $C_P = 224.3$ J/mol-K. The inset shows the temperature dependence of C_P for La_3ZrSb_5 and Ce_3ZrSb_5 in the low temperature region. (b) C_P/T for La_3ZrSb_5 and Ce_3ZrSb_5 are shown. The solid lines represent the linear fit used to obtain the γ and β values.

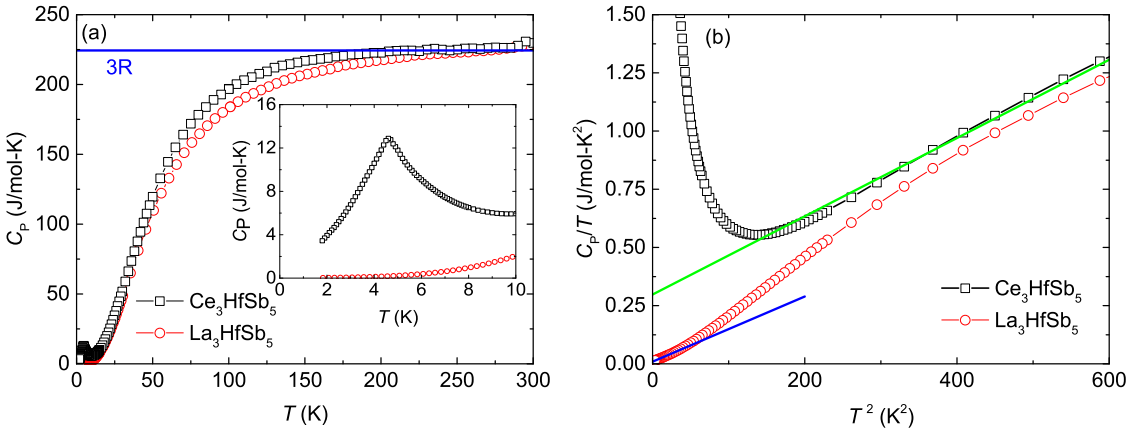

Figure 3.17: (a) The temperature dependence of specific heat $C_P(T)$ for La_3HfSb_5 and Ce_3HfSb_5. The solid line represents the calculated Dulong-Petit limit value, $C_P = 224.3$ J/mol-K. The inset shows the temperature dependence of C_P/T for La_3HfSb_5 and Ce_3HfSb_5 in the low temperature region. (b) C_P/T for La_3HfSb_5 and Ce_3HfSb_5 are shown. The solid lines represent the linear fit used to obtain the γ and β values.

				T_N (K)		
RE_3TMSb_5	γ_{high} (mJ/mol-K^2)	γ_{low} (mJ/mol-K^2)	θ_D (K)	$d\rho(T)/dT$	$d\chi_{ab}(T)/dT$	$C_m(T)$
La_3TiSb_5	-	9.45	223	-		
La_3ZrSb_5	-	10.84	233	-		
La_3HfSb_5	-	9.45	232	-		
Ce_3TiSb_5	275	1460	223	5.2	5.0	5.3
Ce_3ZrSb_5	235	736	213	4.3, 4.7	4.1, 4.8	4.3, 4.7
Ce_3HfSb_5	298	1722	218	4.6	4.6	4.6

Table 3.2: γ and θ_D values and ordering temperature T_N for the grown RE_3TMSb_5 compounds.

300 K. The inset of figure 3.17 (a) shows the low temperature region of C_P to inspect the peak displayed by Ce_3HfSb_5. The peak occurs at $T = 4.6$ K, whereas no peak is seen in La_3HfSb_5. Figure 3.17 (b) shows the C_P/T to show the linear fits conducted to obtain the γ values and Debye temperatures. The obtained values are $\gamma = 298$ mJ/mol-K^2 for Ce_3HfSb_5 and $\gamma = 9.45$ mJ/mol-K^2 for La_3HfSb_5. Debye temperatures of $\theta_D = 218$ and 232 K were obtained for Ce_3HfSb_5 and La_3HfSb_5, respectively. The estimated Debye temperatures for the Hf-based compounds are close to those obtained from Ti- and Zr-based compounds.

Chapter 4

Discussion

At low temperatures, all three Ce-based compounds show signatures of antiferromagnetic (AFM) ordering. The AFM ordering temperature can be determined from different measurements. The feature in magnetic specific heat with simple AFM order is similar to $d\rho/dT$ and $d(\chi T)/dT$ at the ordering temperature [32–35].

Figure 4.1 summarizes the location of the peaks observed in both the magnetic specific heat $C_m(T)$ and the temperature derivative of magnetic susceptibility $d\chi_{ab}(T)/dT$ curves for the Ce_3TMSb_5 compounds, as well as the sharp slope change seen in the temperature derivative of the electrical resistivity $d\rho(T)/dT$. Here, the C_m for the Ce_3TMSb_5 group of compounds is defined as the C_P for Ce_3TMSb_5 subtracted by the C_P for La_3TMSb_5. Ce_3TiSb_5 indicates a peak at $T \sim 5.3$ K in $C_m(T)$, while a minimum at slightly lower temperature $T \sim 5.2$ K in $d\rho(T)/dT$ and a maximum at $T \sim 5$ K in the $d\chi_{ab}(T)/dT$. For the Ce_3HfSb_5 compound, the general trend is very similar to that of Ce_3TiSb_5, with a peak in both $C_m(T)$and $d\chi_{ab}(T)/dT$ at ~ 4.6 K and a minimum in $d\rho(T)/dT$ at at $\sim$ 4.6 K. Since the resistivity of Ce_3TiSb_5 and Ce_3HfSb_5 shows an enhancement below the magnetic ordering temperature due probably to the formation of magnetic superzone gap, the derivative curve doesn't follow well the magnetic part of the specific heat. Ce_3ZrSb_5 behaves differently from the Ti- and Hf-containing samples, where the specific heat displays two visible structures. The location of the slope changes are at $T \sim 4.3$ and 4.7 K, which we define as our T_N values for $C_m(T)$. Similarly to $C_m(T)$, the $d\chi_{ab}(T)/dT$ displays two peaks at $T \sim = 4.1$ and 4.8 K. In contrast to the Ce_3TiSb_5 and Ce_3HfSb_5, the $d\rho(T)/dT$ for Ce_3ZrSb_5 displays a peak at $T = 4.3$ K and a sharp kink at $T = 5$ K. We define the peak position and the location between the peak and sharp kink to be the phase transition temperatures. The determined T_N values for all three of the Ce_3TMSb_5 compounds are summarized in table 3.2.

The determined T_N is lower for both Ce_3ZrSb_5 and Ce_3HfSb_5, in comparison to Ce_3TiSb_5. Referring back to the lattice parameters summarized in figure 2.2, it is noted that the Ce_3TiSb_5, which has the smallest lattice parameters across the Ce_3TMSb_5 samples, re-

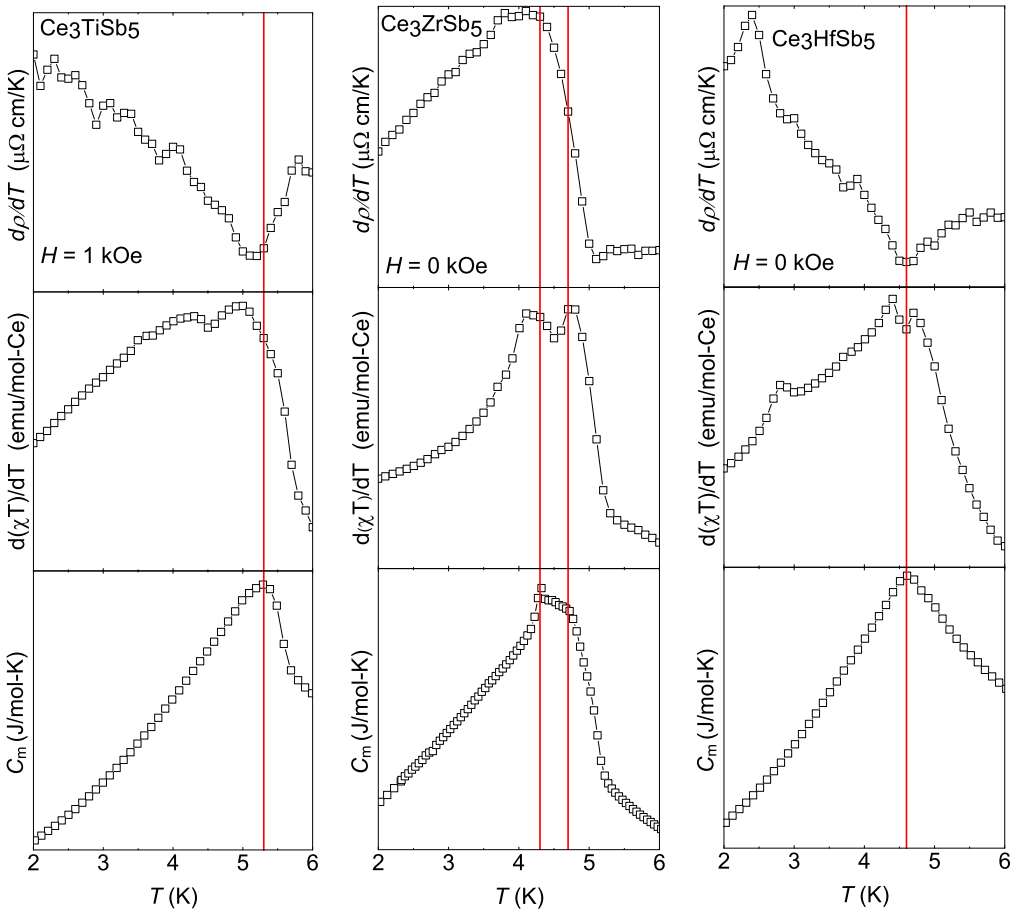

Figure 4.1: The location of anomalies observed in the $d\rho(T)/dT$, $d\chi_{ab}(T)/dT$, and $C_m(T)$ for the Ce_3TMSb_5 compounds. The y-axis is chosen to be arbitrary values. The vertical lines are guided to the eye.

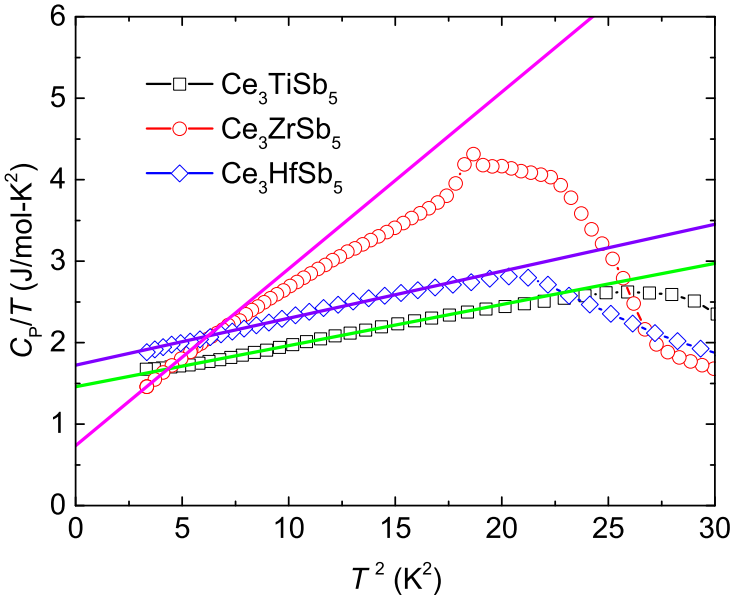

Figure 4.2: The linear fit in T^2 conducted on $C_m(T)/T$ for all three of the Ce_3TMSb_5 (TM = Ti, Zr, Hf) compounds in the low temperature region.

sulted in the highest ordering temperature T_N. When replacing the Ti with Zr, the lattice parameters showed an increase, while replacing the Zr with Hf showed a subtle decrease. In a local moment metallic systems with a simple approximation, the strength of the RKKY interaction is dependent on the distance between magnetic ions within the crystal lattice, which explains the lower T_N values for the Ce_3ZrSb_5 and Ce_3HfSb_5 samples. However, according to the measured lattice parameters (distance between Ce-ions), the T_N for Ce_3ZrSb_5 is expected to be lower than the T_N for Ce_3HfSb_5, but this is not the case. Thus, it has to be considered additional contributions such as Kondo effect.

As seen in the figures 3.14 (a), (b), and (c), each of the Ce_3TMSb_5 compounds display a minimum in the resistivity $\rho(T)$ plots, which is a characteristic observed across Kondo lattice systems [5]. As summarized in table 3.1, the Curie-Weiss temperature θ_p for the Ce_3TMSb_5 are all negative values, indicating that the AFM exchange interaction is dominant. The θ_p value for the polycrystalline average (order of -30 K) is much bigger than the magnetic ordering temperature, which is typical for the Kondo lattice systems. Further, the Kondo effect is evidenced from the specific heat measurement.

The Ce-based compounds all have a high γ value around $\gamma \sim 300$ mJ/mol-K^2, estimated from the high temperature C/T vs T^2 plots (figures 3.15 (b), 3.16 (b), and 3.17 (b)), which is a property of compounds exhibiting the Kondo effect. Since the high temperature specific heat can be affected by the Schottky contribution (discussed below), the γ values are also estimated from the magnetic part of specific heat at low temperatures.

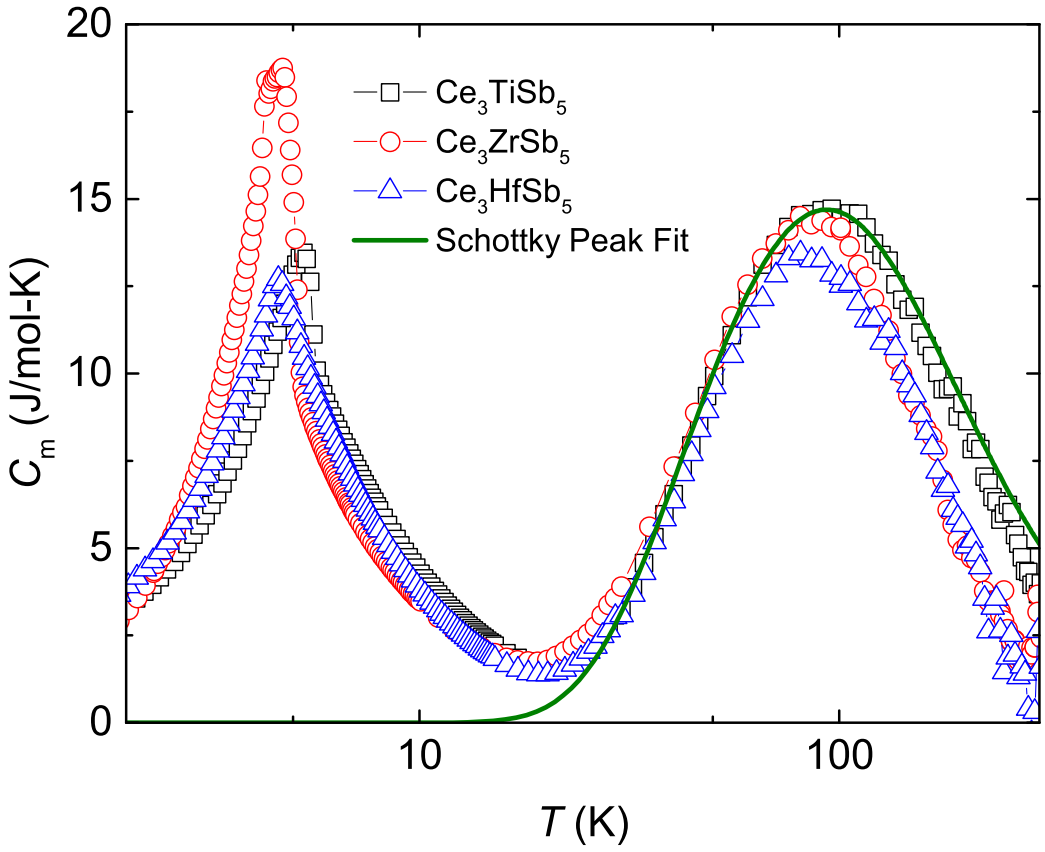

Figure 4.3: The temperature dependence of the magnetic contributions to specific $C_m(T)$ for all three Ce_3TMSb_5 (TM = Ti, Zr, Hf) compounds. The temperature axis is plotted on a logarithmic scale.

Figure 4.2 shows the linear fits conducted on the $C_m(T)/T$ in T^2 below T_N for Ce_3TiSb_5, Ce_3ZrSb_5, and Ce_3HfSb_5. All three of the obtained γ values are $\gamma \sim 1.5$ J/mol-K^2 for Ce_3TiSb_5, $\gamma \sim 0.7$ J/mol-K^2 for Ce_3ZrSb_5, and $\gamma \sim 1.7$ J/mol-K^2 for Ce_3HfSb_5. The γ values extracted from the low temperature specific heat are significantly larger than the high temperature γ values, which can be due to the magnetic contribution below T_N and probably due to the Schottky contribution above T_N. For Ce_3TiSb_5, the C_p/T vs T^2 is linear over the temperature range 0.1 K to 0.4 K, resulting $\gamma \sim 598$ mJ/mol-K^2 [30]. Note that the current specific heat measurement down to 1.8 K for Ce_3TiSb_5 is consistent with earlier report [30]. Thus, it is necessary to perform specific heat measurement below 1.8 K to properly extract the γ value.

Figure 4.3 shows C_m for Ce_3TiSb_5, Ce_3ZrSb_5, and Ce_3HfSb_5 with the temperature axis plotted on a logarithmic scale. The sharp peaks seen in the C_P for the Ce_3TMSb_5 compounds at around $T = 5.3$ K are visible in C_m, with another broad peak centred at $T \sim 100$ K. The sharp peaks at low temperatures are associated with the antiferromagnetic

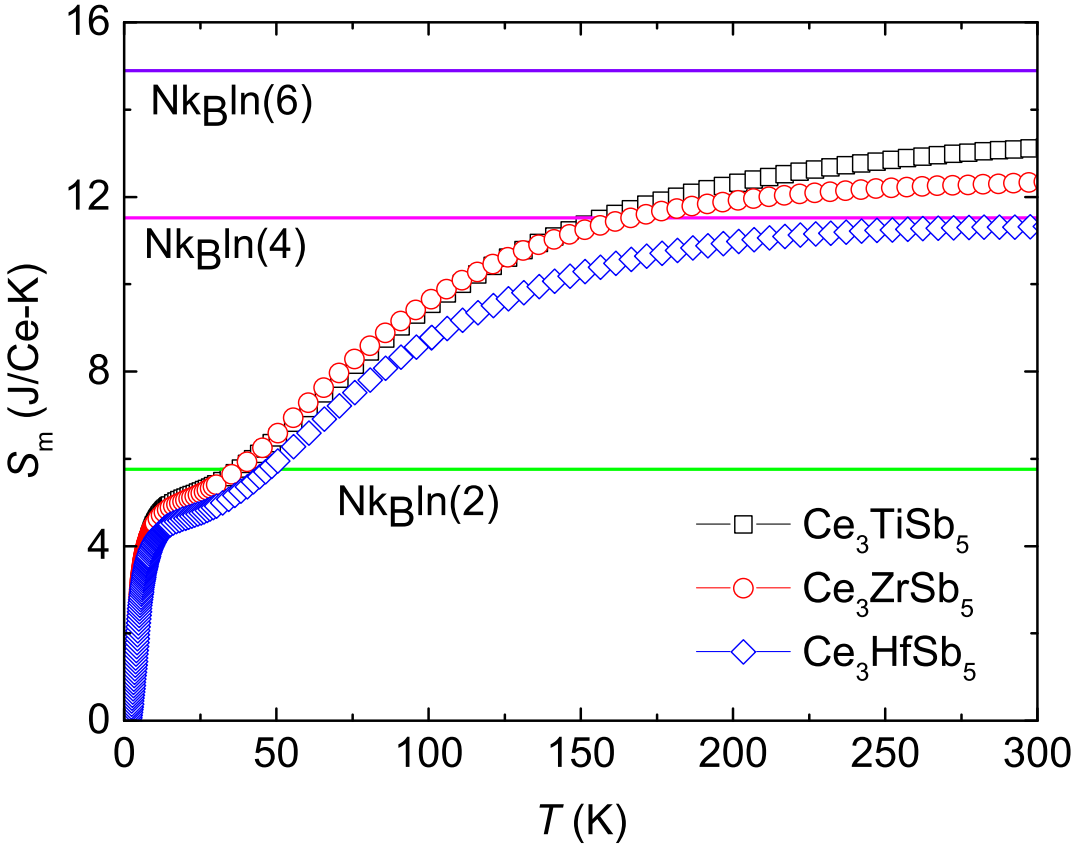

Figure 4.4: The entropy calculated from the magnetic part of specific heat for the Ce_3TMSb_5 compound.

ordering. The high temperature broad peak is a result of the electronic Schottky contributions. By using the equation 1.13, the energy level splitting of the $J = 5/2$ Hund's rule ground state of Ce^{3+} ion is estimated. The solid line in figure 4.3 is a fit curve for Ce_3TiSb_5 with three doublets, where the energy level splittings are $E_1 = 165$ K and $E_2 = 380$ K. We note that the fit was focused on the low-temperature range of the peak, as the high-temperature region is not as reliable, due to amplified subtraction errors. The obtained energy level splittings is in relatively good agreement with the values $E_1 = 178$ K and $E_2 = 336$ K estimated from $\chi(T)$ data in the previous study [30]. The Schottky peak for Ce_3ZrSb_5 and Ce_3HfSb_5 are very close in magnitude and location to the peak observed in Ce_3TiSb_5, indicating that all three compounds present a similar CEF effect.

Figure 4.4 shows the magnetic entropy $S_m(T)$, which is the integral of the C_m/T with respect to T, for the three Ce_3TMSb_5 compounds. The $S_m(T)$ reaches a value of $\sim 0.6R\ln(2)$ at T_N, which is smaller than $R\ln(2)$ expected for a doublet ground state. This lower S_m value at T_N is a clear indication of the Kondo effect. The estimated entropy for all three compounds approaches or slightly exceeds the $R\ln(4)$ around $T = 165$ K, which clearly

indicates the energy level splitting of $J = 5/2$ state due to the CEF effect. The magnetic susceptibility curves for three compounds shows a deviation from the Curie-Weiss law below 150 K, which reflects the contribution from the CEF effect and Kondo interaction.

Chapter 5

Summary

We have grown single crystals of RE_3TMSb_5 (RE = La and Ce, TM = Ti, Zr, and Hf), which crystallize in the hexagonal Hf_5Sn_3Cu-type structure ($P6_3/mcm$). The obtained thermodynamic and transport data show that Ce_3TMSb_5 compounds are antiferromagnetic Kondo lattices with a strong crystalline electric field effect. The magnetic susceptibility measurements indicate that the Ce^{3+} ions are well localized at high temperatures. The specific heat, resistivity, and magnetic susceptibility measurements confirm that all three Ce-based compounds undergo antiferromagnetic transitions below $\sim$5.3 K. All three compounds reveal similar phase transition temperature, implying similar RKKY interaction among the Ce-ions. The Kondo interaction is evident from the $-\log(T)$ dependence in the resistivity and the large negative Curie-Weiss temperature in the magnetic susceptibility. The large γ value in the specific heat suggests that Ce_3TMSb_5 compounds are new heavy fermion compounds. The analysis of the magnetic part of the specific heat confirms that the ground state of title compounds is doublet and well separated from the first and second excited states. We also confirm that the superconducting phase transition in these family arises from the residual Sn flux. For the La_3TMSb_5 compounds, the electrical resistivity shows a broad anomaly at high temperatures. Further measurements are desirable in order to understand the origin of the anomaly.

Bibliography

[1] K. Andres, J. E. Graebner, and H. R. Ott. $4f$-Virtual-Bound-State Formation in $CeAl_3$ at Low Temperatures. *Phys. Rev. Lett.*, 35:1779, 1975.

[2] A. C. Hewson. *The Kondo Problem to Heavy Fermions.* Cambridge University Press, Cambridge, 1997.

[3] F. Steglich, J. Aarts, C. D. Bredl, W. Lieke. D. Meschede, W. Franz, and J. Schäfer. Superconductivity in the Presence of Strong Pauli Paramagnetism: $CeCu_2Si_2$. *Phys. Rev. Lett.*, 43:1892, 1979.

[4] J. G. Bednorz and K. A. Müller. Possible high T_c superconductivity in the Ba-La-Cu-O system. *Z. Phys. B.*, 64(2):189–193, 1968.

[5] G. R. Stewart. Heavy-fermion systems. *Rev. Mod. Phys.*, 56(4):755–787, 1984.

[6] C. L. Seaman, M. B. Maple, B. W. Lee, S. Ghamaty, M. S. Torikachvili, J. S. Kang, L. Z. Liu, J. W. Allen, and D. L. Cox. Evidence for non-Fermi liquid behavior in the Kondo alloy $Y_{1-x}U_xPd_3$. *Phys. Rev. Lett.*, 67:2882, 1991.

[7] G. R. Stewart. Non-Fermi-liquid behavior in d- and f-electron metals. *Rev. Mod. Phys.*, 73:797–855, 2001.

[8] G. R. Stewart. Addendum: Non-Fermi-liquid behavior in d- and f-electron metals. *Rev. Mod. Phys.*, 78:743, 2006.

[9] J. A. Hertz. Quantum critical phenomena. *Phys. Rev. B*, 14:1165, 1976.

[10] A. J. Millis. Effect of a nonzero temperature on quantum critical points in itinerant fermion systems. *Phys. Rev. B*, 48:7183, 1993.

[11] T. Moriya and T. Takimoto. Anomalous Properties around Magnetic Instability in Heavy Electron Systems. *J. Phys. Soc. Jpn.*, 64:960, 1995.

[12] P. Gegenwart, Q. Si, and F. Steglich. Quantum criticality in heavy-fermion metals. *Nat. Phys.*, 4(3):186–197, 2008.

[13] P. Coleman, C. Pépin, Q. Si, and R. Ramazashvili. How do Fermi liquids get heavy and die? *J. Phys.: Condens. Matter*, 13:723–738, 2001.

[14] Q. Si, S. Rabello, K. Ingersent, and J. L. Smith. Locally critical quantum phase transitions in strongly correlated metals. *Nature*, 413:804, 2001.

[15] Q. Si, S. Rabello, K. Ingersent, and J. L. Smith. Local fluctuations in quantum critical metals. *Phys. Rev. B*, 68:115103, 2003.

[16] T. Senthil, M. Vojta, and S. Sachdev. Weak magnetism and non-Fermi liquids near heavy-fermion critical points. *Phys. Rev. B*, 69:035111, 2004.

[17] I. Paul, C. Pépin, and M. R. Norman. Multiscale fluctuations near a Kondo breakdown quantum critical point. *Phys. Rev. B*, 78:035109, 2008.

[18] J. Kondo. Resistance Minimum in Dilute Magnetic Alloys. *Prog. Theor. Phys.*, 32:37–49, 1964.

[19] C.S. Shastry and B.N. Ganguly. On the magnetic susceptibility of Kondo alloys. *Phys. Lett. A*, 29:433–434, 1969.

[20] L. N. Oliveira and J. W. Wilkins. Specific Heat of the Kondo Model. *Phys. Rev. Lett.*, 47:1553, 1981.

[21] N. F. Mott. Rare-earth compounds with mixed valencies. *Philos. Mag.*, 30:403, 1974.

[22] S. Doniach. The Kondo lattice and weak antiferromagnetism. *Phys. B+C*, 91:231–234, 1977.

[23] M. A. Ruderman and C. Kittel. Indirect Exchange Coupling of Nuclear Magnetic Moments by Conduction Electrons. *Phys. Rev.*, 96:99, 1954.

[24] T. Kasuya. A Theory of Metallic Ferro- and Antiferromagnetism on Zener's Model. *Prog. Theor. Phys.*, 16:45–57, 1956.

[25] K. Yosida. Magnetic Properties of Cu-Mn Alloys. *Phys. Rev.*, 106:893, 1957.

[26] K. Binder and A. P. Young. Spin glasses: Experimental facts, theoretical concepts, and open questions. *Rev. Mod. Phys.*, 58(4):801–976, 1986.

[27] C. Kittel. *Introduction to Solid State Physics*. Wiley, New York, 1996.

[28] G. Bollore, M. J. Ferguson, R. W. Hushagen, and A. Mar. New Ternary Rare-Earth Transition-Metal Antimonides RE_3MSb_5 (RE = La, Ce, Pr, Nd, Sm; M = Ti, Zr, Hf, Nb). *Chem. Mater.*, 7(12):2229–2231, 1995.

[29] S. H. D. Moore, L. Deakin, M. J. Ferguson, and A. Mar. Physical Properties and Bonding in RE_3TiSb_5 (RE = La, Ce, Pr, Nd, Sm). *Chem. Mater.*, 14(11):4867–4873, 2002.

[30] M. Matin, R. Kulkarni, A. Thamizhavel, S. K. Dhar, A. Provino, and P. Manfrinetti. Probing the magnetic ground state of single crystalline Ce_3TiSb_5. *J. Phys. Condens. Matter*, 29(14):145601, 2017.

[31] M. J. Ferguson, R. W. Hushagen, A. Mar. Crystal structures of La_3ZrSb_5, La_3HfSb_5, and $LaCrSb_5$. *J. Alloy Compd.*, 249:191–198, 1997.

[32] M.E. Fisher and J.S. Langer. Resistive Anomalies at Magnetic Critical Points. *Phys. Rev. Lett.*, 7:665, 1968.

[33] M.P. Kawatra, S. Skalski, J.A. Mydosh, and J.L. Budnick. Effect of the Molecular Field on the Electrical Resistivity Near a Magnetic Transition: $GdNi_2$. *Phys. Rev. Lett.*, 23:83, 1969.

[34] D.J.W. Geldart and T.G. Richard. Theory of spin-fluctuation resistivity near the critical point of ferromagnets. *Phys. Rev. B*, 12:5175, 1975.

[35] S. Alexander, J.S. Helman, and I. Balberg. Critical behavior of the electrical resistivity in magnetic systems. *Phys. Rev. B*, 13:304, 1976.